Journal of Inorganic Biochemistry 199 (2019) 110758

Contents lists available at ScienceDirect

Journal of Inorganic Biochemistry

journal homepage: www.elsevier.com/locate/jinorgbio

Pd(II) complexes with *N*-heteroaromatic hydrazone ligands: Anticancer activity, *in silico* and experimental target identification

Snežana K. Bjelogrlić[a,b], Tamara R. Todorović[c], Milan Kojić[d], Milan Senćanski[e], Milan Nikolić[c], Aleksandar Višnjevac[f], Jovana Araškov[c], Marija Miljković[d], Christian D. Muller[b], Nenad R. Filipović[g,*]

[a] National Cancer Research Center of Serbia, Pasterova 14, 11000 Belgrade, Serbia
[b] Institut Pluridisciplinaire Hubert Curien, UMR 7178 CNRS Université de Strasbourg, 67401 Illkirch, France
[c] University of Belgrade, Faculty of Chemistry, Studentski trg 12-16, 11000 Belgrade, Serbia
[d] Institute of Molecular Genetics and Genetic Engineering, University of Belgrade, V. Stepe 444a, P.O. Box 23, 11010 Belgrade, Serbia
[e] Center for Multidisciplinary Research, Institute of Nuclear Sciences "Vinča", University of Belgrade, 11000 Belgrade, Serbia
[f] Physical Chemistry Division, Ruđer Bošković Institute, Bijenička c. 54, HR-10000 Zagreb, Croatia
[g] Faculty of Agriculture, University of Belgrade, Nemanjina 6, 11000 Belgrade, Serbia

ARTICLE INFO

Keywords:
Pd(II) complexes
Hydrazones
Apoptosis
Topoisomerase I inhibition
DNA interactions
HSA interactions

ABSTRACT

Anticancer activity of Pd complexes **1–5** with bidentate *N*-heteroaromatic hydrazone ligands was investigated on human acute monocytic leukemia (THP-1; cells in a suspension) and human mammary adenocarcinoma (MCF-7; two-dimensional layer and three-dimensional spheroid tumor model) cell lines. For the Pd(II) complexes with condensation products of ethyl hydrazainoacetate and quinoline-8-carboxaldehyde (complex **1**) and 2-formylpyridine (complex **3**), for which apoptosis was determined as a mechanism of anticancer activity, further investigation revealed that they arrest the cell cycle in G0/G1 phase, induce generation of reactive oxygen species and inhibit Topoisomerase I *in vitro*. *In silico* studies corroborate experimental findings that these complexes show topoisomerase inhibition activity in the micromolar range and indicate binding to a DNA's minor groove as another potential target. Based on the results obtained by circular dichroism and fluorescence spectroscopy measurements, the most active complexes are suitable to be delivered to a blood stream *via* human serum albumin.

1. Introduction

Cancer is the second leading cause of mortality from noninfectious diseases, accounting for 72% of deaths worldwide [1]. Since cancer cells proliferate more rapidly than non-neoplastic ones, the majority of anticancer drugs target the cell cycle by causing a DNA damage [2]. DNA damaging agents can be exogenous or endogenous, physical or chemical, and can damage DNA directly and/or indirectly [3]. The term 'DNA damage' (caused by chemicals) represents any irreversible covalent modification of the DNA molecule, but in a more general sense it includes non-covalent modifications of the DNA structure which also affect DNA replication and transcription [4]. Chemicals such as alkylators and antimetabolites directly target DNA [2], while indirect enzyme mediated DNA damage is a result of inhibition of enzymes involved in the DNA replication process, such as topoisomerases, ribonucleotide reductases and polymerases [5–8].

There is a controversy regarding DNA as an anticancer target. Namely, DNA-targeting chemotherapeutics are not likely to show selectivity between non-neoplastic and cancer cells. On the other hand, a downstream processing of damaged DNA can differ between healthy and cancer cells resulting in a differential cytotoxicity [9]. Nowadays, DNA damaging drugs remain to be center-piece chemotherapeutics regarding new trends in the pharmaceutical industry [10]. The mostly used drugs which target DNA are so called 'platins' - platinum(II)-based complexes that include cisplatin and its six structural analogues which have been approved worldwide for the cancer treatment. Cisplatin is a blockbuster anticancer drug which entered the market exactly half century ago as the first metal-based chemotherapeutic (MBC) [11]. Cisplatin revealed activity against various types of solid tumors [12] and proved especially active against testicular cancer, with a 90% cure rate [13]. For all platinum-based chemotherapeutics which entered the market, DNA was identified as a primary target. Their mechanism of

* Corresponding author.
E-mail address: nenadf@agrif.bg.ac.rs (N.R. Filipović).

https://doi.org/10.1016/j.jinorgbio.2019.110758
Received 14 January 2019; Received in revised form 19 June 2019; Accepted 25 June 2019
Available online 26 June 2019

action includes covalent binding of platinum to DNA bases, with formation of mainly intra-strand cross links, which eventually leads to apoptosis [14]. The importance of these MBCs can be illustrated by the fact that they have been used for the treatment of > 50% cancer patients [15].

The great success of cisplatin in the anticancer treatment, together with a need to overcome its side effects, such as nephrotoxicity and development of tumor resistance, triggered further studies in the medicinal inorganic chemistry to explore for novel MBCs based on platinum and other metals [11,14,16]. Pd(II) complexes have been studied as an alternative to platinum-based complexes due to structural and significant similarity of coordination chemistry of the two metals [15,17]. The important advantage of Pd(II) complexes is at first a better solubility [18], while in the terms of anticancer activity Pd(II) complexes have shown comparable or even improved activities than approved platinum-based and other approved chemotherapeutics, with reduced cross-resistance and decreased toxicity [15,17,19]. On the other hand, Pd-complexes are more reactive and can undergo a spontaneous *cis-trans* isomerization. Because of high reactivity, Pd-based MBCs are often unable to reach their biological targets, while isomerization of active *cis* into *trans* isomers results most frequently in decreased activity. An effective strategy for prevention of isomerization is use of NN' chelating ligands for preparation of Pd(II) based MBCs [18].

In our previous study, we investigated a cytotoxic action of several Pd(II) complexes with bidentate N-heteroaromatic chelators (complexes **1–4**, Scheme 1), which are the condensation products of ethyl hydrazinoacetate hydrochloride (haOEt × HCl) and quinoline-8-carboxaldehyde (q8a), quinoline-2-carboxaldehyde (q2a), 2-formylpyridine (py2a) and 2-acetylpyridine (py2ac). The activity of the complexes was evaluated on human promyelocytic leukemia (HL-60), human glioma (U251), rat glioma (C6), and mouse fibrosarcoma (L929) cell lines [19]. Our results revealed that Pd complexes with q8ahaOEt and q2ahaOEt (Scheme 1) reduced the cell numbers in a dose-dependent manner for the investigated cell lines. The observed antiproliferative effect of the complexes was predominantly mediated through the induction of apoptotic cell death. Among investigated complexes, the complex with q8ahaOEt ligand appeared to be the most effective with the activity comparable to cisplatin in all the investigated cell lines.

The goal of our present work is to get a deeper insight into the mechanism of action of these Pd(II) complexes, complemented with a novel pyridine-based Pd(II) complex with *N*-heteroaromatic hydrazone ligand py2bzhaOEt (complex **5**, Scheme 1).

2-Benzoylpyridine (py2bz) based hydrazones are known for their potent anticancer activity [20–26]. Their cancer relevant targets include Bcl-2 (B-cell lymphoma 2) [24], Fe-dependent histone demethylase KDM4A [25], ribonucleotide reductase [26,27] and thiol-reductase [27]. On the other hand, Pd(II) complexes with py2bz-based hydrazones may manifest more favorable type of cell death than corresponding ligands [28]. Some Pd(II) complexes showed better activity than corresponding ligands, like Pd(II) complex derived from 2-benzoylpyridine N^4-phenylthiosemicarbazone [29]. Also, Pd(II) complexes of py2bz-based hydrazones act as inhibitors of relevant cancer targets; for example, Pd(II) complex with 2-benzoylpyridine N4-ethylthiosemicarbazone inhibits Rce1p protease [30]. In order to get a deeper insight into molecular target(s) of the most active Pd(II) complexes from the library, we applied a combination of experimental and *in-silico* studies.

2. Experimental

2.1. General remarks

The chemicals $K_2[PdCl_4]$ (min 32.0% Pd), py2bz (99 + %), py2ac (99 + %), py2a (99%) and q2a (97%) were obtained from Acros Organics, while haOEt × HCl (97%) was obtained from Fluka. Q8a (97%) was obtained from Maybridge. All solvents (reagent grade) were used without further purification. Elemental analyses (C, H, N, S) were performed by the standard micro-methods using an ELEMENTAR Vario ELIII CHNS = O analyzer. Molar conductivities were measured at room temperature (25 °C) on a multimeter MM41 (Crison). IR spectrum of novel Pd-complex (Fig. S1, Supplementary material) was recorded on a Thermo Scientific Nicolet 6700 FT-IR spectrophotometer by the Attenuated Total Reflection (ATR) technique in the region 4000–400 cm^{-1}. Abbreviations used for IR spectrum: *vs*, very strong; m, medium; w, weak. UV–Vis spectrum (Fig. S2, Supplementary material) was recorded at room temperature on a NanoDrop 2000c spectrophotometer (Thermo Scientific, USA) equipped with 1.0 cm quartz cell. All NMR spectral measurements were performed on a Bruker Avance III 500 spectrometer equipped with a broad-band direct probe. The spectra were recorded at room temperature in DMSO-d_6. Chemical shifts are given on δ scale relative to tetramethylsilane as internal standard for ^1H and ^{13}C. Coupling constants (J) were expressed in Hz. Abbreviations used for NMR spectrum: d, doublet; t, triplet; q, quartet; m, multiplet; dd, doublet of doublets; td, triplet of doublets; ddd, double double doublet. 1D (^1H and ^{13}C) and 2D (COSY, NOESY, ^1H–^{13}C HSQC and ^1H–^{13}C HMBC) spectra are shown in Figs. S3–S8 (Supplementary material). The atom numbering for the ligand py2bzhaOEt was given in Scheme S1 (Supplementary material).

2.2. Synthesis of [$PdCl_2$(q8ahaOEt)] (1), [$PdCl_2$(q2ahaOEt)] (2), [$PdCl_2$(py2ahaOEt)]·DMSO (3) and [$PdCl_2$(py2achaOEt)] (4)

The complexes **1–4** were prepared by template reactions of $K_2[PdCl_4]$, 8qa/q2a/py2a/py2ac and haOEt × HCl, as described previously [19]. IR and NMR spectroscopy data, as well as molar conductivity measurements and results of elemental analysis for the complexes **1–4** are in good agreement with the data previously published.

2.3. Synthesis of [$PdCl_2$(py2bzaphaOEt)] (5)

A solution of haOEt × HCl (0.054 g, 0.46 mmol) and py2bz (0.084 g, 0.46 mmol) in 15 mL of ethanol was stirred at 40 °C for 1 h and then 2 mL of water solution of $K_2[PdCl_4]$ (0.15 g; 0.46 mmol) was added. The

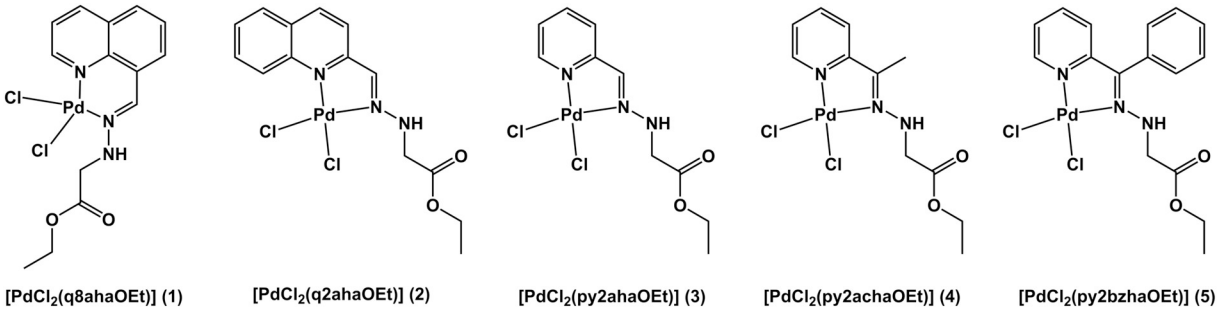

Scheme 1. Structures of the complexes **1–5**.

mixture was stirred at 40 °C for 1 h. During reaction a yellow precipitate was formed. The precipitate was separated by filtration, washed by small portions of the following cold solvents: water, ethanol and diethyl ether. Yellow single crystals were obtained after recrystallization from acetonitrile. Yield: 0.16 g (73%). Anal. Calcd. for $C_{16}H_{17}N_3O_2Cl_2Pd$ (%): C, 41.72; H, 3.72; N, 9.12. Found: C, 41.59; H, 3.59, N, 9.12. Λ_M (2.17×10^{-3} M, DMSO) = 5.81 Ω^{-1} cm^2 mol^{-1}. IR (ATR, ν_{max}/cm^{-1}): 3244 (m), 1743 (s), 1586 (s), 1205 (*vs*), 1024 (w). UV/Vis (DMSO, $c = 1.4 \times 10^{-4}$ mol dm^{-3}), λ: 332 nm. ^{1}H NMR (500.26 MHz, DMSO-d_6) δ: 1.13 (t, 3H, C11−H, $^3J_{11,10}$ = 7.1 Hz), 3.52 (d, 1H, C8−H, $^3J_{8,N3H}$ = 5.8 Hz), 4.04 (q, 1H, C10−H, $^3J_{11,10}$ = 7.1 Hz), 7.05 (dd, 1H, C3−H, $^3J_{3,4}$ = 7.9 Hz, $^4J_{3,5}$ = 1.1 Hz), 7.56–7.52 (m, 2H, C13−H and C13′–H), 7.67–7.61 (m, 3H, C14−H, C14′–H and C15−H), 7.70 (ddd, 1H, C5−H, $^3J_{5,4}$ = 7.9 Hz, $^3J_{5,6}$ = 5.7 Hz, $^4J_{3,5}$ = 1.1 Hz), 8.02 (t, 1H, N3−H, $^3J_{N3H,8}$ = 5.8 Hz), 8.11 (td, 1H, C4−H, $^3J_{4,3} = {}^3J_{4,5}$ = 7.9 Hz, $^4J_{4,6}$ = 1.3 Hz), 8.99 (dd, 1H, C6−H, $^3J_{6,5}$ = 5.7 Hz, $^4J_{6,4}$ = 1.3 Hz). ^{13}C NMR (126.0 MHz, DMSO-d_6) δ: 13.11 (C11), 51.36 (C8), 61.14 (C10), 126.02 (C3), 126.16 (C5), 129.07 (C13 = C13′), 129.52 (C15), 129.9 (C12), 131.11 (C14 = C14′), 141.3 (C4), 149.64 (C6), 155.48 (C7), 157.6 (C2), 167.69 (C9).

2.4. X-ray crystallography

Crystal data, data collection and refinement parameters are summarized in Table S1 (Supplementary material). Data collection was performed at room temperature on an Oxford Diffraction Xcalibur Nova R diffractometer with a micro-focusing Cu tube (λ = 1.54180 Å). Data reduction and cell refinement were carried out using the CRYSALIS PRO software [31]. Structures were solved by direct methods with SIR2014 [32] and refined by a full matrix least-squares refinement based on F2, with SHELXL [33]. Molecular illustrations were prepared with ORTEP-3 [34] and MERCURY [35] included into the WinGX package [36]. Calculations of molecular geometries and crystal packing parameters were performed with PLATON [37]. All H-atoms with the exception of H15 (attached to N15) were included in their geometrically calculated positions and refined according to the riding model, while H15 was located in the Fourier map and refined freely. CCDC 1847413 contains the supplementary crystallographic data. These data can be obtained free of charge *via* http://www.ccdc.cam.ac.uk/conts/retrieving.html, or from the Cambridge Crystallographic Data Centre, 12 Union Road, Cambridge CB2 1EZ, UK; fax: (+44) 1223-336-033; or e-mail: deposit@ccdc.cam.ac.uk.

2.5. Evaluation of biological activity and molecular docking studies

Detailed protocols for anticancer related experiments (annexin V and propidium iodide staining, calculation of $ApoC_{50}$/$ApoC_{25}$ concentrations, cell cycle analysis, inhibition of caspase activity, evaluation of caspase-8 and -9 activities, determination of mitochondrial superoxide generation, assessment of changes in mitochondrial potential and growth inhibition of 3D tumor models), human serum albumin (HSA) interaction experiments, molecular docking to HSA, DNA and Topoisomerase I (Top I) and II (Top II), Top I activity inhibition assays, interactions with plasmid DNA, and acute lethality assay, can be found in Supplementary material.

3. Results and discussion

3.1. Anticancer experiments

3.1.1. Complexes *1* and *3* revealed as more potent apoptosis inducers than cisplatin

In our previous work we tested antiproliferative activity of complexes **1–4** on a palette of four cancer cell lines by means of 3-(4,5-dimethylthiazol-2-yl)-2,5-diphenyltetrazolium bromide (MTT) [19]. The MTT, as other colorimetric assays, gives the information whether the applied treatment reduces the number of viable cells in respect to non-treated control over the time of incubation, but does not provide the insight on the mode of investigated complexes' activity. According to those results [19], **1** and **2** reached the IC_{50} values on all four cell lines, where **1** revealed as more potent. The least efficient was **4** that did not achieve significant reduction of cell viability in any of treated cell lines. In the current investigation, we took a different approach, testing the incidence and types of cell death after the same incubation time as previously [19]. Two human cell lines, mammary adenocarcinoma (MCF-7) and acute monocytic leukemia cells (THP-1), used in the present study were exposed to complexes **1–5** applied in a range of six concentrations, and after 24 h were assessed by means of Annexin V/propidium iodide (PI) dual staining method. Therefore, we were here able to evaluate the exact ability of investigated complexes to initiate either apoptotic or necrotic death in THP-1 and MCF-7 cell lines. Percentages of Annexin V single-stained and double-stained cells are summarized for each concentration of investigated complexes and plotted against corresponding concentration. The $ApoC_{50}$ or $ApoC_{25}$ concentrations are computed as those that correspond to 50% and 25% of apoptotic events on concentration-response curve, respectively.

Among hereby tested complexes, **1** and **3** are the two that triggered exclusively apoptotic response in THP-1 cells (Fig. 1A). On this cell line, **2** and **4** induce necrotic death in significant percentage, while **5** does not have noteworthy activity (data not shown). Both, **1** and **3**, do not stimulate significant incidence of cell death at concentrations of 1 and 10 μM. At 30 μM, **1** challenges apoptosis but almost all those events are Annexin V single-stained, whereas treatment with **3** at the same concentration leads THP-1 cells already toward late phases of apoptotic death. Percentage of cells in advanced phase of apoptosis increases with increasing concentration of **1** and **3**. However, while the vast majority of cells subjected to **3** at 75 and 100 μM are double-stained, more than one third of cells treated with **1** at the same concentrations are non-stained with either Annexin V or PI. Such difference in pro-apoptotic activity of those two complexes on THP-1 cells is clearly visible when comparing their concentration-response curves (Fig. S11, Supplementary material). While both complexes achieved almost equal $ApoC_{50}$ value, the upper plateau in the curve for **1** starts at concentration of 50 μM, whereas exponential phase in the curve for **3** is extending up to concentration of 100 μM. This result is particularly interesting from the point of our previously published data where **3** did not reveal noteworthy antiproliferative activity against another leukemia cell line [19].

Contrary to the THP-1 cell line consisting of cells with identical phenotype, MCF-7 cell culture is a conglomeration of distinctive phenotypes differing in gene expression profile [38]. This phenomenon is in correlation with a recently reported feature of breast cancer cells that re-establish phenotypic equilibrium of parental tumor bulk, under laboratory conditions, instead of breeding a cloned cell population [39]. Thereby, although it is regularly seen that the same compound has various effect on different cell lines, in case of breast cancer cells the response to treatment can vary within the same tissue culture flask. For those reasons, the presence of necrotic events in treated THP-1 cells can indicate on certain degree of toxicity, whereas dual mode of death in MCF-7 cells can be interpreted as a result of diverse modules of interaction between investigated compound and treated phenotypes.

Regarding activity of investigated complexes in MCF-7 cells, complexes **1** and **3** are the only that achieve apoptosis, while the amplitude of apoptotic response between those two complexes is inverse compared to that in THP-1 cells (Fig. 1B). In the MCF-7 samples treated with **1** from 50 to 100 μM, almost all acquired events are double-stained. On the other hand, in the MCF-7 samples subjected to **3**, concentration-dependent increase in incidence of double-stained cells is found in the samples incubated with concentrations from 50 μM and higher, whereas live cells are still present in the specimen subjected to 100 μM. Nevertheless, the difference in sensitivity of THP-1 and MCF-7 cells to treatments with **1** and **3** is easier to observe comparing

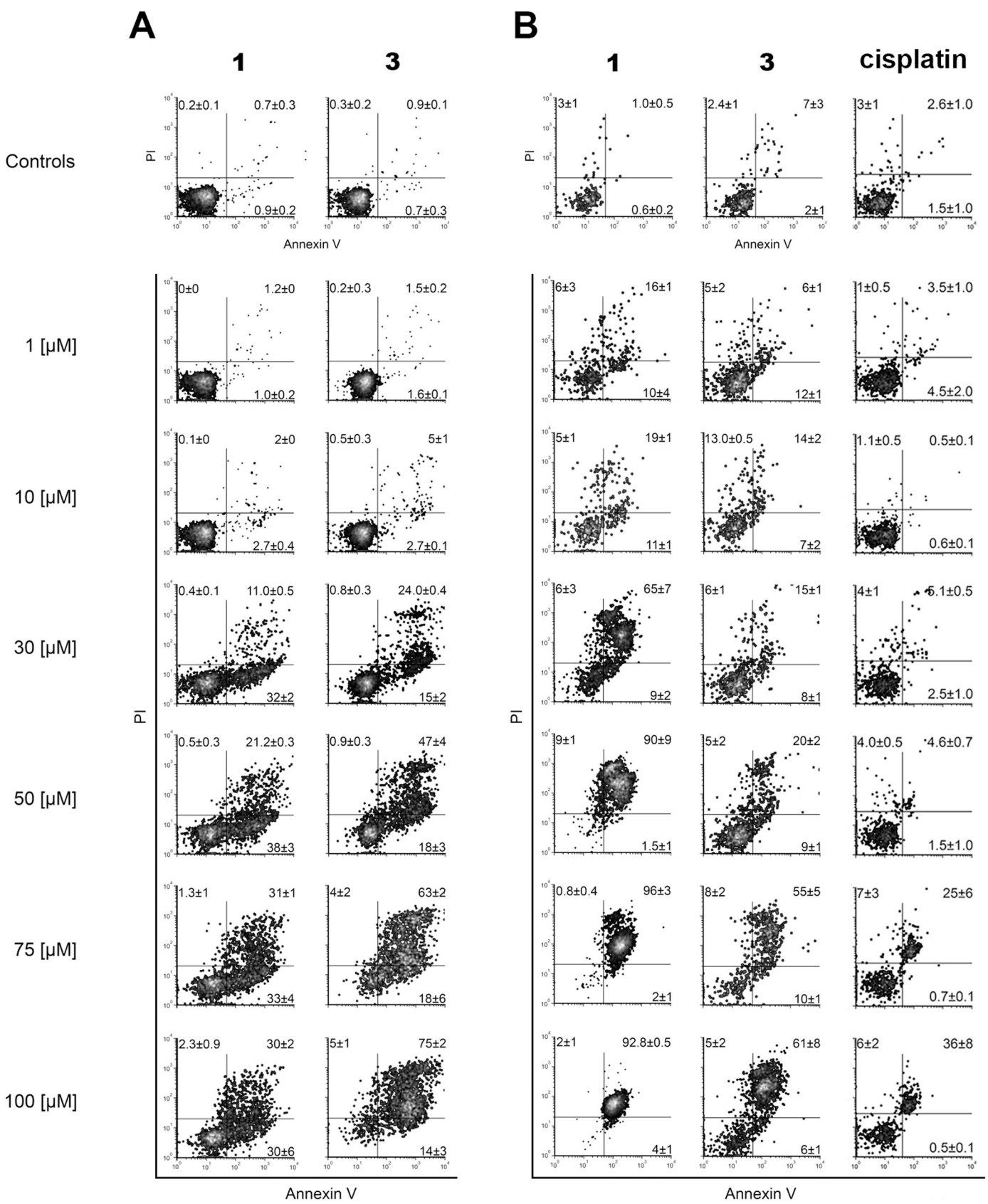

Fig. 1. Different types of cell death in THP-1 (A) and MCF-7 (B) cells treated with investigated complexes. The types were determined by means of Annexin V/PI assay after 24 h incubation. In Annexin V/PI dot plots cells are discriminated as viable (non-stained cells, lower left quadrant), cells in early phase of apoptotic death (Annexin V single-stained cells, lower right quadrant), cells in advanced phases of cell death (double-stained cells, upper right quadrant), and necrotic cells (PI single-stained cells, upper left quadrant). Results are represented as the mean ± SD percentages of two replicates from independent experiments.

concentration-response curves and achieved $ApoC_{50}$ values (Fig. S11A and S11B, Supplementary material). Activity of **1** in MCF-7 cells is described by the curve with gradually inclining exponential phase, while reached $ApoC_{50}$ concentration is notably lower compared to that determined in THP-1 cells. On the contrary, concentration-response curve for **3** at MCF-7 cells has steeply positioned exponential phase with the maximal average percentage of dead cells reached at 75 μM (Fig. S11B, Supplementary material). Additionally, the $ApoC_{50}$ concentration of **3** in MCF-7 cells is 1.8-fold higher than for THP-1 cells. Contrary to **1** and **3**, their corresponding ligands, q8ahaOEt and py2ahaOEt, demonstrate trivial activity on THP-1 and MCF-7 cells, respectively (Fig. S12, Supplementary material).

Study of the activity of cisplatin in THP-1 cells [40] revealed that over 24 h of incubation an extensive apoptotic response is induced, but majority of cells remain in initial phase of programmed death. Such delayed initiation of apoptosis could be explained by known mechanism of cisplatin's activity which propels activation of a complex network of DNA repair pathways in order to preserve genomic integrity [2,41]. According to those earlier published data [40], computed $ApoC_{50}$ concentration that cisplatin achieved on THP-1 cells is 17 ± 1 μM, making cisplatin to seem as a more powerful agent than here investigated **1** and **3**. However, **1** and particularly **3** drive THP-1 cells through the whole process of apoptotic death within the same period of incubation (Fig. 1A), which is opposite to the effect achieved with cisplatin [40]. Here, MCF-7 cells, that we previously described as relatively resistant to cisplatin compared to other breast cancer cell lines [42], do not respond with a significant incidence of cell death till a cisplatin concentration of 75 μM (Fig. 1B). Since cisplatin does not reach 50% of apoptotic events at tested range of concentrations, the $ApoC_{25}$ concentration has been computed and implemented in further evaluation (Fig. S11C, Supplementary material). In summary, our results clearly show that **1** and **3** reveal as more potent inducers of apoptosis in THP-1 and MCF-7 cells than cisplatin.

In preliminary toxicity screening, *in vivo* acute lethality of **1–5** and cisplatin were tested on brine shrimp *Artemia salina* after 24 h incubation. LC_{50} values for **1–5** (> 0.416 ± 0.085 mM) were significantly higher than for cisplatin (0.006 ± 0.002 mM), which indicates that cisplatin induces higher incidence of lethality in comparison to investigated Pd(II) complexes. Therefore, it can be anticipated that **1–5** would possess the lower acute toxicity potential in comparison to cisplatin.

3.1.2. Cell cycle changes indicate that *1* and *3* interfere with DNA replication

An altered distribution of cells throughout phases of mitotic division, *vs.* non-treated samples, represents the initial indication of the interference of the investigated drug in the cellular process. Although mechanisms responsible for accumulation of cells within any particular phase of cell cycle may be numerous, such results provide rationale for decision which way further investigations should be directed to. Here, we applied technical solution to assess cell cycle distribution in the same specimens that were previously analyzed for apoptosis, thus all possible inconsistencies due to separate courses of incubations were reduced to a minimum, which enables direct observation of correlations between cell death incidence and alterations in arrangement of cells within phases of mitotic division.

For THP-1 and MCF-7, cell cycle distributions assayed for cells treated by **1** share common characteristics (Fig. 2A). In both cell lines, accumulation at the G0/G1 phase is the dominant feature. While for THP-1, the greatest cell percentage is reached in samples subjected to **1** at 50 μM with no further significant variations up to 100 μM, in MCF-7 cells frequency of cells at the G0/G1 phase is gradually intensifying in concentration-dependent manner. On the contrary, treatment with **3** has diverse impact on these two cell lines. In THP-1 cells, **3** stimulates cells gathering at the S phase starting from the concentration of 30 μM, which at higher concentrations turns into accumulation at the G1-to-S check point (Fig. 2A). However, in none of THP-1 samples subjected to **3,** percentages of cells at the G2/M phase are found as significantly reduced compared to non-treated control. This finding indicates that treated THP-1 cells are just delayed in passing though G1-to-S or S phase, without development of the cell cycle arrest. Accumulation at the S phase is also seen in MCF-7 cells but already at 1 μM of **3**. From concentration of 50 μM, mostly all MCF-7 cells are shifted toward G1-to-S checkpoint. While for THP-1 cells accumulation at the S phase coincided with significant rise in percentages of events in early and advanced phases of apoptotic death (Figs. 1A and 2A), apoptosis in MCF-7 cells is not triggered till cells aggregated at the G1-to-S check point (Figs. 1B and 2A). Those results do not necessarily indicate that **3** exerted different mode of activity on THP-1 and MCF-7 cells, but rather on dissimilar degree of sensitivity and response of these two cell lines to treatment with the same compound.

Changes in the cell cycle distribution of THP-1 cells treated with cisplatin were reported previously [40]. Briefly, after cell agglomeration at the G2/M and S phase seen in samples treated with cisplatin at 1 and 3 μM, respectively, cell cycle distribution was shifted toward accumulation at the G1-to-S check point starting from samples subjected to cisplatin at 10 μM. Apoptosis occurred simultaneously with appearance of G1-to-S cell cycle arrest, and both events were intensifying coincidentally with increase of cisplatin's concentration. Analogous changes are found here in MCF-7 cells. In the samples subjected to cisplatin at 1–30 μM, cells accumulated at the G2/M phase (Fig. 2A) that is accompanied with the absence of cell death events (Fig. 1B). Starting from cisplatin at 50 μM, percentage of cells within G2/M phase becomes significantly reduced, whereas cisplatin at 75 and 100 μM stimulates assembling of treated cells at the S phase. Therefore, while THP-1 cells agglomerate at the G1-to-S checkpoint, which is an indication of prevention of the beginning of chromosomal replication, MCF-7 cells pass this control spot and enter into the S phase. This finding might be confusing knowing that MCF-7 cells have wild-type p53, which is not the case with THP-1 cells [43,44]. However, other authors recognized similar dichotomy in response of p53+/+ and p53−/− cells to treatment with cisplatin [45,46]. Also, it should be noted that the G1-to-S checkpoint can be activated p53-independently [47], which can be of importance for interpretation of results acquired in THP-1 and MCF-7 cells after treatment with **1** and **3**, in the context of their putative pro-apoptotic mechanisms.

3.1.3. Complex *3* challenges independent activation of intrinsic and extrinsic apoptosis pathways in both treated cell lines

It was previously determined that **1** induced significant activation of caspase-3 in HL60 cells [19]. In the current study, we assessed the degree of apoptosis dependence on caspase activation (results presented in Supplementary material), and pattern of caspase-8 and caspase-9 activation, which provide us with more detailed insight regarding transduction of apoptotic signaling in cells treated with **1** and **3**.

A fundamental difference is found between THP-1 and MCF-7 cells regarding constitutive activation of two major apoptotic pathways (Fig. 2B). In THP-1 non-treated samples, percentage of cells with single-activated caspase-9 is the dominant event. On the contrary, MCF-7 cells display basic activation of caspase-8 followed by a subsequent caspase-9 cleavage (double-stained cells). The existing cross-talk pattern between extrinsic (caspase-8) and intrinsic (caspase-9) apoptotic pathways allows their mutual activation [48,49]. While intrinsic pathway can drive cells throughout the whole process of apoptotic death, all on its own, two cell types were determined regarding events following the activation of caspase-8, irrespective of how caspase-8 had been activated (due to triggering of death receptor signaling cascade [50], or by means of endoplasmic reticulum (ER) stress [50–52]). In so-called type 1 cells that have the ability to produce large amounts of active caspase-8, activated extrinsic pathway can lead the cell throughout the course of apoptosis independently of caspase-9. In the type 2 cells, such as MCF-7 cells are, extrinsic apoptotic signal has to be augmented by activation of

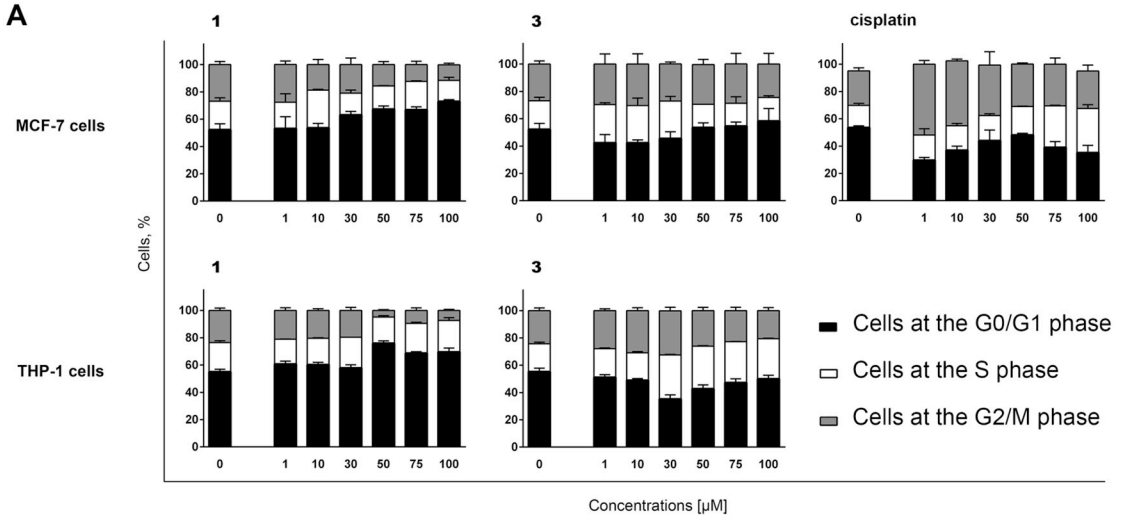

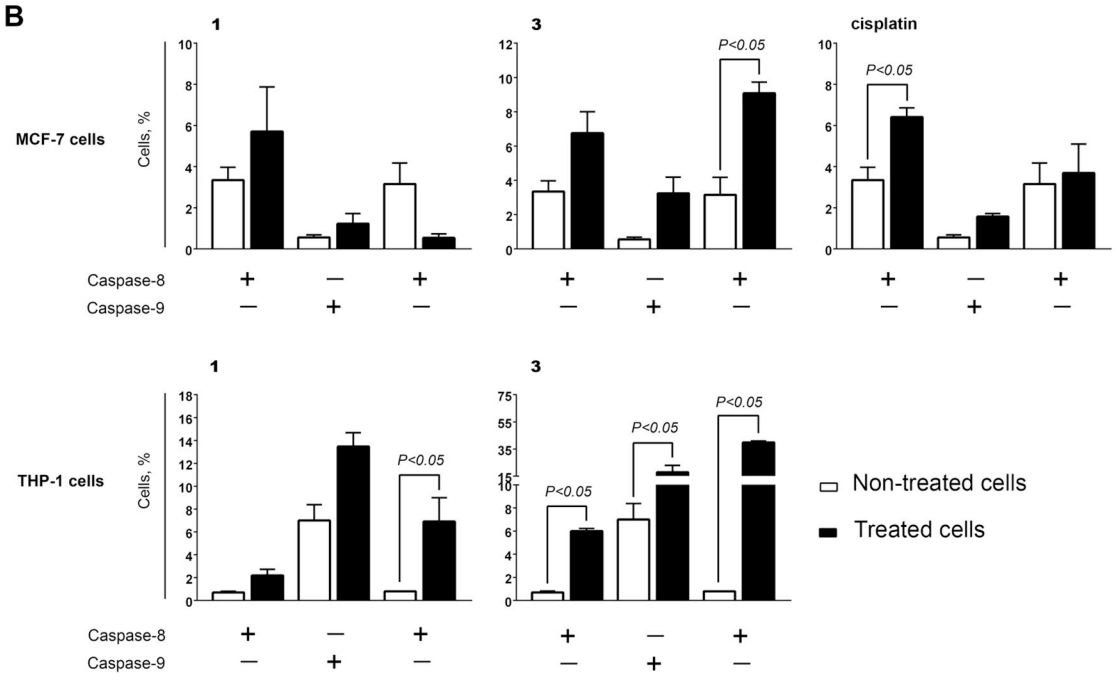

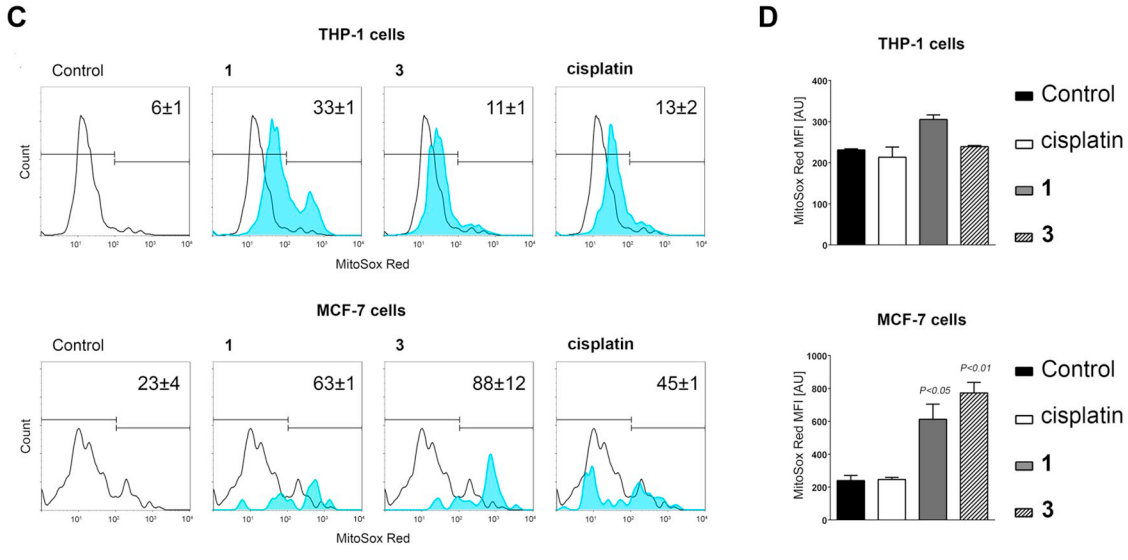

(caption on next page)

Fig. 2. (A) Cell cycle distribution of cells induced by treatment with investigated complexes. Results are expressed as the mean ± SD percentages of two replicates from independent experiments. (B) Percentages of cells with activated caspase-8, caspase-9 or both activated caspases determined after 6 h incubation with investigated complexes. Results are represented as the mean ± SD of three replicates from independent experiments. Statistical evaluation has been performed using unpaired *t*-test with Welch's correction comparing treated to non-treated populations. (C) Mitochondrial superoxide ($O_2\cdot^-$) generation in cells determined by means of MitoSox Red staining after 6 h treatment with investigated complexes. Results are represented as the mean ± SD of three replicates from independent experiments. (D) Median fluorescent intensity (MFI) expressed in arbitrary units (AU), computed for $O_2\cdot^-$-positive subpopulation. Results are presented as the mean ± SD of three replicates from independent experiments. Statistical evaluation has been performed using Kruskal-Wallis test with unpaired *t*-test with Welch's correction as posttest.

intrinsic pathway and caspase-9.

As we previously described, cisplatin treatment did not induce significant activation of either caspase-8 or -9 in THP-1 cells [40]. Considering known mechanism of cisplatin activity, we assumed that caspase-2 was accountable for triggering of apoptotic death. Capsase-2, which beside caspase-8 and -9 is another activator caspase, has been reported to be involved in apoptotic response induced by multiple intrinsic and extrinsic stimuli such as DNA damage, reactive oxygen species (ROS) and cytoskeletal disruption [53]. Active caspase-2 can further cleave BH3 interacting-domain death agonist (Bid) protein and propels intrinsic apoptotic pathway activation [54]. In terms of Bid cleavage, caspase-2 is far less efficient compared to caspase-8, thus low levels of active caspase-2 may not cleave enough of Bid to provoke intrinsic apoptotic pathway in the absence of complementary pro-apoptotic signals [55]. It was demonstrated that caspase-2 is a substrate for caspase-8 and -3, but *vice versa* interactions has not been affirmed yet [56]. Additionally, MCF-7 cells constitutively express high level of antiapoptotic B-cell lymphoma 2 (Bcl-2) protein, which may suppress cytochrome *c* release consequently to processing of Bid [57,58]. This distinctive characteristic of MCF-7 cells may be used to explain the omission of double-stained cells in the samples assayed for caspase-8 and -9 activities after treatment with cisplatin, although active caspase-8 is found as significantly up regulated (Fig. 2B).

Complex **1** in THP-1 samples stimulates quite analogous patterns of caspase-8 and -9 activation, and cell cycle changes (Fig. 2A and B) to that we previously published for cisplatin [40]. According to these results, it can be postulated that **1** and cisplatin may share some common features in mechanism of their anticancer activities in THP-1 cells that are related to DNA replication process. Similarity between patterns of caspase-8 and -9 activations in samples subjected to **1** and cisplatin is remaining in MCF-7 cells too (Fig. 2B). However, accumulation of MCF-7 cells at the S phase seen in samples treated with **1** at low concentrations is also found after treatment with cisplatin, but at 75 and 100 μM. It is particularly interesting that treatment of MCF-7 cells with **1** notably down-regulates cross-talk activation of intrinsic pathway that is not affected in cells incubated with cisplatin (Fig. 2B). Therefore, **1** and cisplatin do not display striking resemblance in response of MCF-7 cells, contrary to here found for THP-1 samples.

Quite the opposite, a significant augmentation in percentages of events with both activated caspase pathways are found in the THP-1 and MCF-7 samples treated with **3**, together with subpopulations that express single-activated either caspase-8 or -9 (Fig. 2B). This particular result indicates that **3** triggers at least two pro-apoptotic mechanisms in both cell lines, where each of them initiates downstream cascades that are conducted irrespective of each other. This result additionally supports assumption that **3** exerts dual mode of activity.

*3.1.4. Generation of reactive oxygen species (ROS) may be presumed as the main mechanism of **1** activity in MCF-7 cells*

While mechanism of Pd complexes' activity has been far less studied compared to complexes with other transition metals, their anticancer properties are address the induction of double strand brakes, ER stress, and ROS [59]. In recently published study, mitochondria are confirmed as important sub-cellular target in Pd toxic profile [60]. Results showed that inorganic Pd, applied as Pd(II) chloride, in concentrations lower than 100 μM had no significant effect on isolated mitochondria. At higher concentrations (100–400 μM) there was a concentration- and time-dependent increase in mitochondrial ROS production. It was revealed that Pd interacts directly with the F_1-F_0 ATP synthase, which is sometimes referred to as "Complex V", *via* dissipation of proton-motive force and consequential failure in ATP production [60]. Furthermore, increased mitochondrial ROS formation and oxidation of membrane protein thiol groups caused opening of mitochondrial permeability transition pores (PTPs), followed by unlimited proton leakage across the inner mitochondrial membrane, mitochondrial swelling, and uncoupling of oxidative phosphorylation [61]. Those results, however, cannot be taken as relevant in context of here investigated organic Pd complexes due to few reasons. First, organic ligands with coordinated Pd can, and do drastically increase lipophilicity and effective permeability compared to Pd salt [62]. Second, the ability of coordinated complex to undergo ligand exchange reactions offers numberless opportunities for metals to interact and coordinate with other biological molecules [59]. However, recognition of mitochondrion as the key cellular organelle in Pd toxicity connotes that mitochondria also may have the important role in mechanism of Pd complex's anticancer activity. For those reasons we tested ability of **1** and **3**, together with cisplatin as a reference drug, to generate production of mitochondrial superoxide radicals ($O_2\cdot^-$) and induce changes in mitochondrial transmembrane potential (MTP) in THP-1 and MCF-7 cells.

It was previously confirmed that cisplatin accumulates in mitochondrion and forms adducts with mitochondrial DNA (mtDNA) and proteins [63,64]. Since mitochondria are lacking nucleotide excision repair (NER) pathway, adducts on mtDNA cannot be removed contrary to those in nuclear DNA [63]. Work of Marullo et al. [65] showed that mitochondrial generation of ROS, within several hours after cisplatin was added on cells, is not correlated to mtDNA damage. However, after 24 h of treatment, cisplatin-induced mitochondrial ROS production arises as a consequence of mtDNA transcription block caused by formed mtDNA adducts. Transcription block leads to reduction of protein synthesis and impair the functioning of electron transport chain. Other groups reported on increased expression of ROS scavenging enzymes in cisplatin-resistant cells compared to sensitive ones [66–68].

Measurement of mitochondrial $O_2\cdot^-$ following a short-term incubation, as it was performed in our investigation, indicates on $O_2\cdot^-$ production, caused by interaction of investigated complexes with mitochondrial proteins [69]. Possible role of mtDNA adducts might contribute to apoptotic response that was estimated after 24 h treatment, but that supposition could not be assessed by experimental method used in the current study. Therefore, here revealed results should be discussed in terms of two crucial parameters: $O_2\cdot^-$ generation flow, and efficacy of $O_2\cdot^-$ neutralization. The rate of $O_2\cdot^-$ production is defined by concentration of the enzyme that serves as electron carrier, concentration of electron donor (investigated complex) established within mitochondrion, and second-order reaction between them [69]. The main route for $O_2\cdot^-$ elimination is its dismutation to hydrogen peroxide (H_2O_2) by means of superoxide dismutase (SOD) enzyme. Out of three SOD isoforms present in mammalian cells that are localized within different subcellular compartments, two of them are strategically stored in mitochondria. Thus, manganese SOD (MnSOD, or SOD2) is restricted to mitochondrial matrix, while copper/zinc SOD (Cu/Zn SOD, or SOD1) is localized within mitochondrial intermembrane space and cellular cytoplasm [70]. There are no available literature data that

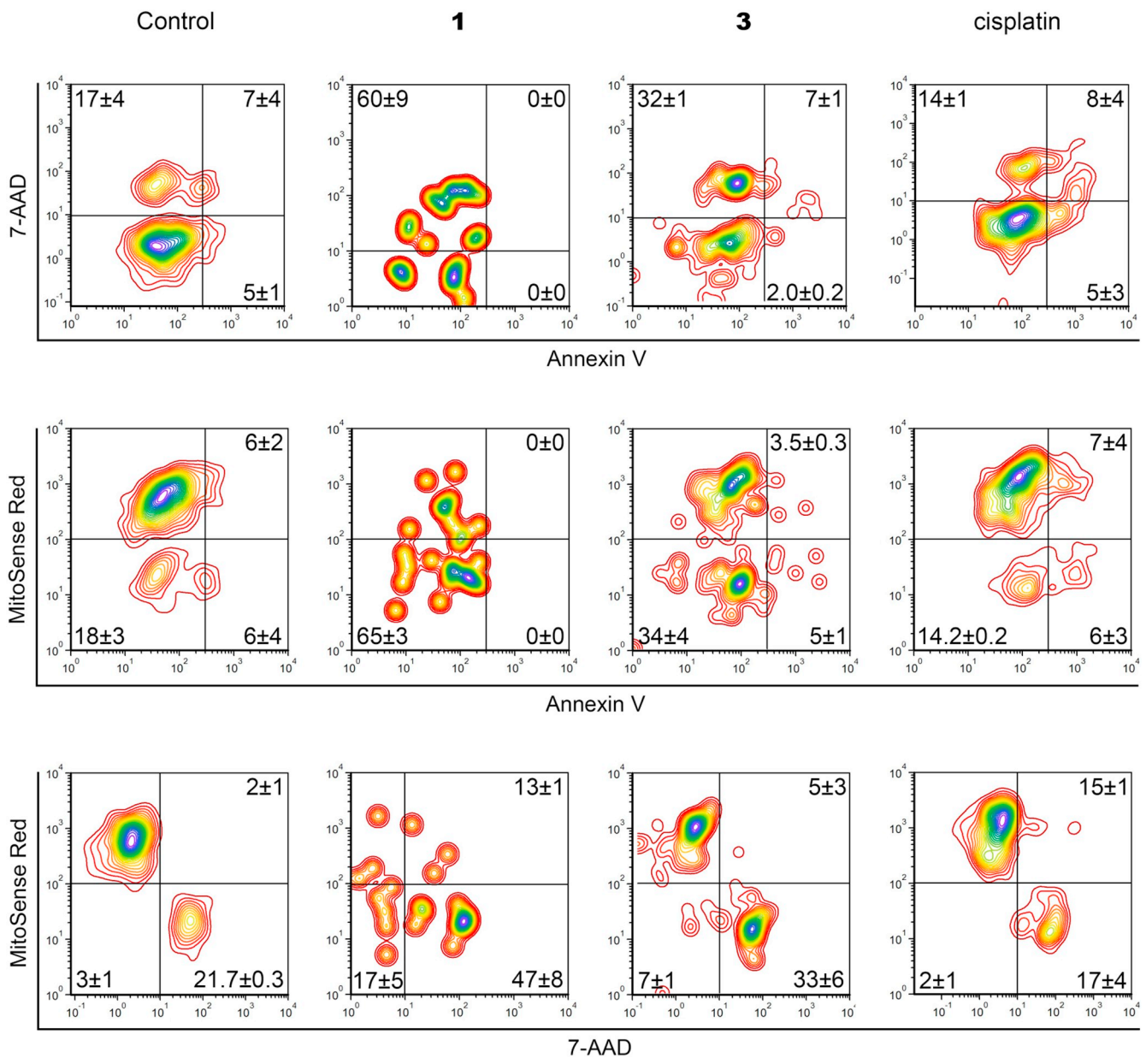

Fig. 3. Dissipation of MTP in MCF-7 cells, non-treated and treated with investigated complexes for 6 h, determined by Mitosense Red/Annexin V/7-Aminoactinomycin D (7-AAD) staining. In the upper panels cells are discriminated according to the type of cell death (non-stained viable cells and stained with Annexin V and/or 7-AAD). In the middle panels cells are discriminated according to staining with Mitosense Red dye (negative cells in lower left and right quadrants have scattered MTP) and concomitant staining with Annexin V (apoptotic cells in upper right and lower right quadrants). In the lower panels cells are discriminated according to staining with Mitosense Red dye and concomitant staining with 7-AAD (cells in necrosis or advanced phase of apoptosis in the upper right or lower right quadrants). All results are presented as the mean ± SD percentages of two replicates from independent experiments.

demonstrate malfunctions in SOD1 or SOD2 expression levels and/or activities in THP-1 cells. On the contrary, MCF-7 cells are reported for reduced expression level and activity of SOD2, together with lower expression level of mitochondrial fraction of SOD1 compared to another human breast cancer cell line MDA-MB-231 [71]. Furthermore, MCF-7 cells were shown to have significantly higher uncoupled respiration than human mammary epithelial cells MCF-10A [72]. The respiratory chain uncoupling implies the proton leak without ATP production, which consequently leads to lowering of electrochemical potential across the inner mitochondrial membrane with increased mitochondrial respiration rate and $O_2\cdot^-$ production [73]. In the current work, there is notable difference considering percentages of $O_2\cdot^-$-positive events in non-treated controls of MCF-7 and THP-1 samples (Fig. 2C). The MFI expressed in arbitrary units (AU) indicates on median density of fluorescently marked target of interest per cell, in this case median flow of newly generated $O_2\cdot^-$ per cell (Fig. 2D). Therefore, notably higher incidence of $O_2\cdot^-$-producing cells in MCF-7 compared to THP-1 non-treated samples is accompanied with slightly increased median $O_2\cdot^-$ flow at the MCF-7 cellular level (231 ± 3 AU and 240 ± 38 AU in THP1 and MCF-7 cells, respectively).

In THP-1-treated samples, cisplatin and **3** cause modest increase in percentage of $O_2\cdot^-$-generating cells (Fig. 2C) followed with no obvious aberration regarding MFI values compared to non-treated control (Fig. 2D). Complex **1** shows the highest pro-oxidant activity in THP-1 cells, scoring 5.5-fold increase in $O_2\cdot^-$-positive subpopulation, but elevation of mitochondrial $O_2\cdot^-$ flow per cell is statistically insignificant. In MCF-7 cells, **1** causes < 3-fold increase of $O_2\cdot^-$-positive subpopulation compared to control. Cisplatin doubles the percentage of

$O_2\cdot^-$-producing MCF-7 cells, whereas **3** provokes the greatest rise in percentage of $O_2\cdot^-$-generating cells. Similarly to what has been seen in THP-1 cells, cisplatin in MCF-7 samples does not enhance $O_2\cdot^-$ flow per cell, while both **1** and **3** reach significantly higher MFI values in MCF-7 cells. As is noted above, Pd was reported for ability to preferably target complex V of the mitochondrial respiratory chain, thus impairing electron transfer and ATP production [60]. However, necrosis that results as the consequence of significantly depleted ATP level [74] is just a minor event in MCF-7 cells as evidenced by means of Annexin V/PI assay after 24 h treatment with either **1** or **3**. This may indicate that Complex V probably was not targeted by investigated complexes. In order to provide better insight into course of events at the level of mitochondria in MCF-7 cells, we further performed evaluation of MTP using the same experimental conditions as for estimation of mitochondrial $O_2\cdot^-$ generation.

Significant increase in mitochondrial $O_2\cdot^-$ production drives a series of events that can lead the cell toward apoptotic or necrotic death. Under physiological conditions, mitochondrial $O_2\cdot^-$ are generated at respiratory complexes I and III [75]. Majority of them are dismutated by SOD2, while the rest are released into mitochondrial intermembrane space and after in cytoplasm through mitochondrial permeability transition pores (PTPs) [76]. PTPs have been recognized as the main target of mitochondrial ROS [77]. It is known that $O_2\cdot^-$ can oxidize thiol groups located in the PTP's matrix site and thereby modulate their opening [78]. The PTP opening can be either transit or permanent, whereas the latter event involves a rapid increase of mitochondrial permeability with consequent matrix swelling and dissipated MTP (dMTP) [78,79]. Several research groups revealed that dMTP appears shortly after PTPs opening, while others showed that dMTP is rather caspase-dependent process than directly related to the state of PTPs [79]. Those data indicate on the possibility of two pathways, in a first dMTP occurring in an early phase of apoptosis and being caspase-independent, while in the other MTP is not affected until apoptotic death was not initiated. Finally, dMTP causes a rapid interruption in ATP synthesis. If cellular ATP level drops beneath 50% the cell undergoes necrosis, while apoptosis is likely to occur when ATP level remains relatively high [74].

There is noteworthy difference between samples subjected to our investigated complexes considering percentages of cells positive for dMTP (Fig. 3). After incubation with cisplatin, the incidence of MCF-7 cells that display dMTP is slightly below the level in non-treated controls (20 ± 2% and 24 ± 1% for cisplatin-treated and non-treated samples, respectively). Interestingly, in the samples subjected to **1** and **3**, inverse correlation is found between results on flow of $O_2\cdot^-$ production incidence of dMTP-positive cells (Fig. 3). While **3** triggers stronger $O_2\cdot^-$-producing response than **1** considering both percentages and MFI values, proportion of cells that are displaying dMTP following treatment with **3** is lower (40 ± 5%) than in the samples incubated with **1** (64 ± 2%). Furthermore, in **1**-treated samples 13 ± 1% cells are stained with 7-Aminoactinomycin D (7-AAD) but have no dMTP, while 17 ± 5% of cells that show dMTP are not labeled with either 7-AAD or Annexin V. Incidence of dead events that are concomitantly negative for dMTP afterward incubation with **3** is very low (4 ± 1% and 4.4 ± 1.5% for **3**-treated and non-treated samples, respectively).

Overall, our current results indicate that $O_2\cdot^-$ generation is important mechanism in activity of **1**. As reviewed above, complex **1** triggers death in more than a half of treated MCF-7 cells already after 6 h of incubation (Fig. 3), while almost the same percentage of cells is positive for mitochondrial $O_2\cdot^-$ (Fig. 2C). Concentration of **1** applied in experiments on MCF-7 cells for evaluation of $O_2\cdot^-$ and dMTP is 2.5-fold higher than $ApoC_{50}$ after 24 h treatment (Fig. S11B, Supplementary material). At $ApoC_{50}$ there is no significant activation of neither caspase-8 or − 9 in MCF-7 samples subjected to **1** (Fig. 2B), while initiation of apoptotic death is revealed as highly caspase-dependent process (Fig. S13, Supplementary material). Similar responses regarding activation of extrinsic and intrinsic caspase pathways are seen in THP-1 cells (Fig. 2B), while **1** at 1.4-fold higher concentration than $ApoC_{50}$ induces greater $O_2\cdot^-$ production compared to **3** and cisplatin (Fig. 2C). In both, THP-1 and MCF-7 cells, a treatment with **1** launched accumulation of cells at the G0/G1 phase of mitotic division (Fig. 2A). Therefore, according to current data, together with notable similarity in patterns of caspase activation and cell cycle changes between **1** and cisplatin reviewed above, it is quite possible that **1** exerts two mechanisms of activity. One of those mechanisms overrules in THP-1 cells, which have well-functioning antioxidant defense. That mechanism implies caspase-dependent apoptosis possibly by initially activated caspase-2 due to interfered process of DNA replication. Another mechanism is disclosed in MCF-7 cells and comprises powerful pro-oxidant activity of **1** that leads to development of dMTP in majority of treated cells already after short-time incubation (Fig. 3). However, accumulation of MCF-7 cells at the S phase after treatment with **1** at 10 μM implies that the mechanism proposed as likely responsible in THP-1 cells is launching in MCF-7 cells too, although at low concentration level. At higher concentrations of **1**, $O_2\cdot^-$ production with consequent dMTP become dominant events in MCF-7 cells and causes cell cycle block at the G0/G1 phase, quite contrary to cisplatin (Figs. 2A, C and 3).

On the other hand, **3** in MCF-7 cells challenges greater $O_2\cdot^-$ production than **1** (Fig. 2C and D), although pro-oxidant capacity of **3** on MCF-7 cells was tested at concentration lower than its $ApoC_{50}$ (Fig. S11B, Supplementary material). At the same time, only half of $O_2\cdot^-$ positive subpopulation also displays dMTP (Fig. 3), which strongly indicates that **1** and **3** interact with different electron carriers within mitochondrion where the former probably attacks some of the enzymes within respiratory chain. Furthermore, **3** induces quite different pattern of caspase activation than **1** and cisplatin on both cell lines (Fig. 2B). Complex **3** in THP-1 cells stimulates activation of intrinsic and extrinsic apoptotic pathways independently of each other, which suggests that **3** arouses two different mechanisms of activity at the very same moment (Fig. 2B). Similar result is evident in MCF-7 samples as well (Fig. 2B). According to cell cycle changes, treatment with **3** probably compromises DNA replication process in both treated cell lines (Fig. 2A). However, activation of intrinsic apoptotic pathway, which is related to significant metabolic distress, cannot be addressed to generation of mitochondrial $O_2\cdot^-$ in THP-1 cells since those are revealed as less susceptible to pro-oxidant activity than MCF-7 cells (Fig. 2B and C). The reason why about a half of $O_2\cdot^-$-positive MCF-7 subpopulation does not display dMTP and statistically significant activation of intrinsic caspase pathway should be investigated in further studies.

*3.1.5. Complex **1** achieves superior inhibition of MCF-7 spheroids' growth than other tested complexes*

One of the major challenges modern scientists face with in drug research and development considers the use of inappropriate experimental models that are raising false conclusions. Caused consequences do not include only significant scientific errors, but also the major increase in cost of studies since majority of drugs that passed basic laboratory evaluation fail during early phases of clinical investigations [80]. The main reason for such overwhelming statistics is the gap between morphology and physiology of standardly employed two-dimensional (2D) monolayer cell models compared to tumor tissue in body, which significantly lowers the predictive reliability the expected clinical benefit according to laboratory results. Those are the reasons three-dimensional (3D) models have been developed, becoming a useful surrogate model for estimation of drug effect on growth of tumor bulks [81]. Number of studies demonstrated that 3D models, contrary to 2D cells, highly resemble tumor tissue regarding intercellular interactions, cell proliferation, differentiation, gene and protein expression, and cellular response to drug treatment and other external stimuli [82–85].

Here, treatment of MCF-7 3D cultures with **1** or **3** result with different effects in terms of spheroids' growth rate and morphological features. In non-treated controls, spheroidal growth is accompanied with expansion of necrotic core and consequential narrowing of

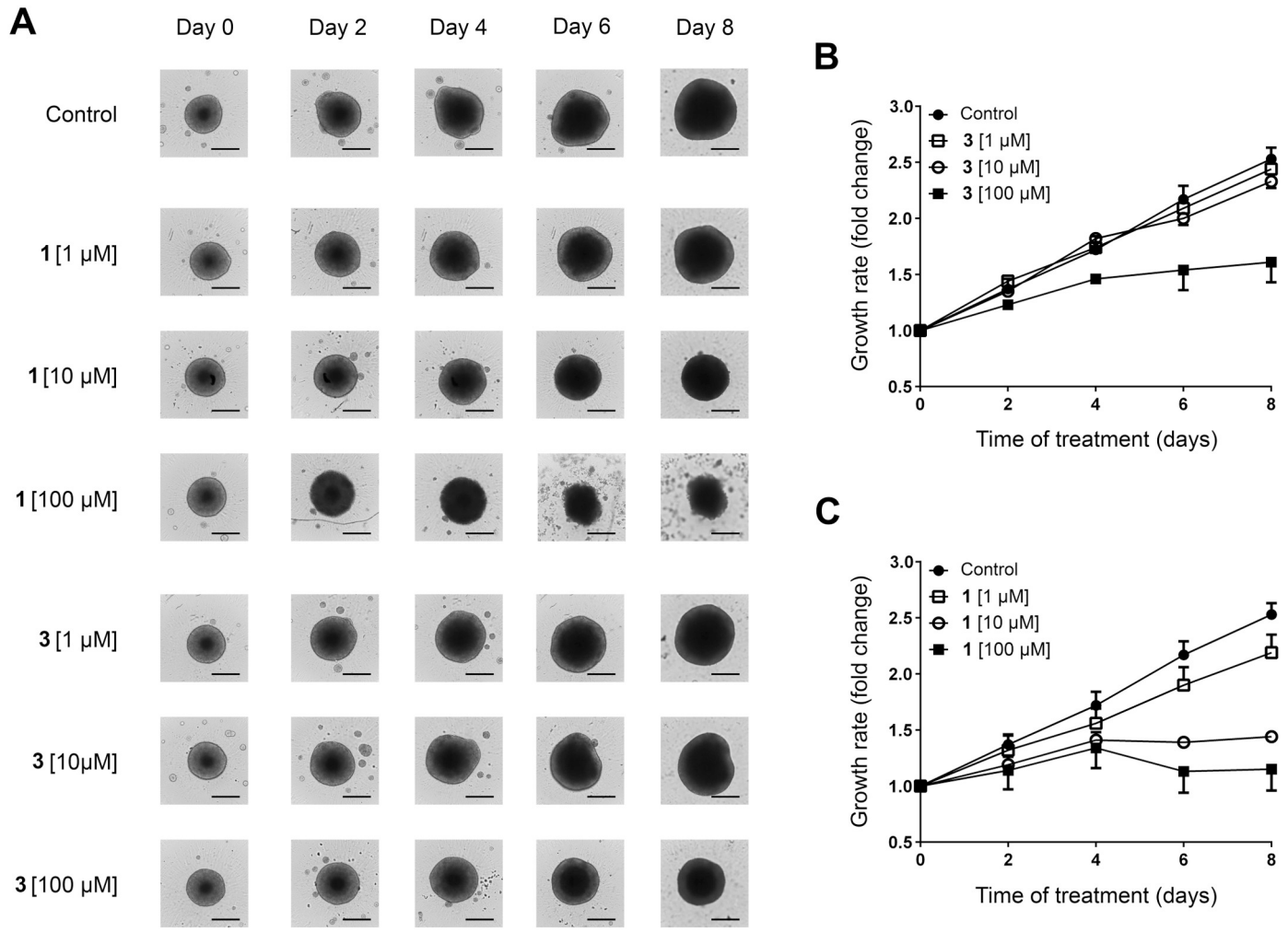

Fig. 4. Changes in size and morphology of MCF-7 3D spheroids over the 8 days of treatment with investigated complexes (A). Images have been taken every other day on Celigo imaging cytometer using Celigo software. Scale bar: 200 μm. Growth rate graphs for MCF-7 3D spheroids non-treated and treated with **3** (B) or **1** (C). Results are represented as the mean fold change ± SD of two replicates from independent experiments.

quiescent zone, where both are clearly distinctive till the day 6 (Fig. 4A). At the day 8, quiescent zone becomes opaque and appears as merged with necrotic core, while the border between those two sections gets blurred and hardly recognizable. 3D samples subjected to **3** at concentrations of 1 and 10 μM are displaying morphological features very similar to non- treated controls. The only difference is that at the day 8 proliferative zones in treated spheroids can be visually distinguished from necrotic core, similarly to non-treated 3D tumors on the day 6. According to growth rate values, **3** at 1 and 10 μM does not achieve noteworthy delay in size increase compared to controls (Fig. 4B). At the day 8, size of control spheroids increased for 2.5 ± 0.1 fold compared to the day 0, while the growth of treated samples is barely decelerated (2.44 ± 0.04 fold and 2.3 ± 0.1 fold of increase for tumors treated with **3** at 1 and 10 μM, respectively). Complex **3** at 100 μM has more impact regarding both observed parameters. During the first four days of incubation, spheroids subjected to 100 μM record a moderate gain in size (Fig. 4B). During that time, their morphology is not crucially different compared to spheroids treated with **3** at other two lower concentrations, with exception of noticeably smaller necrotic core and wider quiescent zone (Fig. 4A). On the half course of incubation time, **3** at 100 μM achieves considerable growth delay of 3D tumors, with 1.6 ± 0.2 fold in size increase on the day 8. Moreover, in those spheroids at the day 6, necrotic core is separated from proliferation zone with clearly distinctive rime that remained preserved until the end of the experiment.

Morphological modifications in 3D MCF-7 models induced by treatments with **1** are more diversifying between three tested concentrations than those reviewed in spheroids subjected to **3**. Complex **1** at 1 μM did not achieve significant changes either in growth (2.2 ± 0.2 fold at the day 8, Fig. 4C) or morphology of treated 3D samples (Fig. 4A). However, compared to non-treated samples, proliferative zone in those spheroids is significantly wider and pellucid even on the last day of the experiment. Quite the opposite, in 3D tumors treated with **1** at 10 μM, quiescent zone seems as completely merged with necrotic core at the day 6. The rugged rim of those spheroids at the day 8 indicates that cells within proliferation zone are promptly dying. At the very beginning of treatment, proliferation zone is razed in spheroids subjected to **1** at 100 μM (Fig. 4A). In the same samples, quiescent zone is dark and dimmed while necrotic core remains almost the same size as on the day 0 of treatment. Described morphological changes, which indicate on accelerated cell death, are progressing till the day 4, but 3D tumors still have a spheroidal shape. Extensive destruction of 3D tumor mass by **1** at 100 μM leads to shredding of spheroidal structure, with debris scattering around the remaining tumor mass. It is interesting that **1** at concentrations of 10 and 100 μM has almost the same effect on growth of 3D spheroids up to the day 4 when **1** at 10 μM completely arrests their growth while at 100 μM it additionally reduces the size of treated samples (Fig. 4C). Precisely, the size of spheres subjected to **1** at 100 μM at the day 8 records only 1.1 ± 0.2 fold of overall increase compared to the day 0. Furthermore, **1** at 10 μM gains better result than

3 at 100 μM (1.44 ± 0.03 and 1.6 ± 0.2 fold increase, respectively). To draw a comparison with previously published results on the same experimental model, carried under the same experimental conditions [86], treatment with cisplatin achieves almost the same growth control at 10 and 100 μM on the day 8 (1.0 ± 0.1 and 0.9 ± 0.3 fold increase, respectively), and 1.8 ± 0.5 fold increase at 1 μM. A parallelism between modes of cisplatin and **1** activities reviewed above can also be outlined here by comparing alterations in morphological attributes of spheroids subjected to cisplatin [86] and **1** (Fig. 4A).

Although **2**, **4**, and **5** do not display significant pro-apoptotic activity on MCF-7 2D model, we decided to test their ability to restrain growth of 3D spheroids using the same experimental protocol as that applied for evaluation of **1** and **3**. In a separately organized experiment, one replicate per concentration of those complexes was treated, together with three replicates of non-treated controls. Control samples showed higher growth rate in respect to experiment carried out for **1** and **3** (Fig. 4), with 3.1 ± 0.3 fold increase in size at the day 8 (Fig. S14, Supplementary material). Surprisingly, each of three here assessed complexes reveal antitumor activity on 3D model, but in a different extent. Thus, spheroids subjected to **2**, **4** and **5** at concentration of 100 μM show 1.2, 1.5 and 1.8 fold increase in size, respectively. Those results firmly confer superiority of 3D models compared to standard monolayer cultures in investigation of new drug's activity. Relying on the current 3D data, complexes that were discarded due to lack of apoptotic response assessed on 2D model deserve additional experimental evaluation for anticancer activity in further studies.

3.2. Spectroscopic studies revealed binding of *1* and *3* to human serum albumin (HSA)

HSA (66.5 kDa) is an essential extracellular protein with a high concentration in blood (about 60% of the total amount of plasma proteins) and with an extraordinary binding capacity for various endogenous and exogenous ligands, including drugs. Crystal structure analyses have revealed that this heart-shaped α-helical protein has binding sites for most aromatic and heterocyclic ligands mainly located within two hydrophobic pockets in subdomains IIA (Sudlow's site I) and IIIA (Sudlow's site II) [87].

UV absorption spectroscopy is used to investigate protein-ligand complex formation. As a typical protein, HSA has a characteristic absorption band located in the range of 260–300 nm, originating from the absorbance of the aromatic amino acids (Trp, Tyr, and Phe). As can be seen in Fig. 5A, the strong absorbance of HSA with a pick at 278 nm decreased with the addition of **1** or **3**, indicating an interaction between HSA and Pd–complexes.

Fluorescence spectroscopy is a simple but effective method to detect and characterize the interactions between metal complexes and serum albumins. The intrinsic Trp and Tyr residues of HSA can emit fluorescence, and ligand binding usually induces quenching of protein fluorescence. Fig. 5B shows the typical fluorescence emission spectra of HSA in the presence of various concentrations of **1** or **3**. It was observed that the fluorescence intensity of protein decreases regularly with the increasing concentration of both ligands, and the quenching provoked by the Pd-complexes is significant (up to 52% of the initial fluorescence intensity at 340 nm for **1** and 70% for **3**).These data indicate that Pd-complexes are likely to interact with HSA *via* a hydrophobic region located inside the protein and quench its intrinsic fluorescence [88].

The type of fluorescence quenching (static or dynamic) can be distinguished by their different dependence on temperature or preferably by life time measurements [89]. Fig. S15A (Supplementary material) represents the Stern-Volner (SV) plots for the HSA fluorescence quenching by **1** and **3** at three different temperatures. Almost perfect linear correlation coefficients ($R > 0.999$) indicate that the quenching of HSA by Pd-complexes could be interpreted by the SV equation. As the quenching constant decreases with increasing temperature for both ligands, and the values of k_q are much greater than the limiting diffusion rate constant of the biomolecule ($2 \times 10^{10}\ M^{-1}\ s^{-1}$; Table 1), it can be concluded that a static (contact) type of quenching occurs. The calculated binding constant of $1.1 \times 10^5\ M^{-1}$ for **1** and $1.6 \times 10^5\ M^{-1}$ for **3** at 25 °C indicates specific binding for Pd-ligands on HSA. In comparison with drugs and other exogenous compounds, observed binding constants of the order of magnitude $10^5\ M^{-1}$ are among the moderate ones [90]. The number of binding sites in HSA approximates to 1 (Table 1), indicating that only one site is reactive to Pd-complexes in the experimental setup similar to physiological condition.

Synchronous fluorescence spectra can provide information on the molecular microenvironment, particularly in the vicinity of the fluorophore functional groups. Fig. S15B and S15C (Supplementary material) illustrate representative synchronous fluorescence spectra of HSA with various amounts of **1** and **3** recorded at $\Delta\lambda = 60$ nm (Trp) and $\Delta\lambda = 15$ nm (Tyr), respectively. The maximum emission wavelengths of Trp and Tyr residues remain practically unchanged during the interaction, implying that the polarity around these two amino acid residues is retained. In comparison with Tyr, a much stronger fluorescence quenching of Trp is observed on the addition of Pd–ligands, especially **3**. Trp-214 is the only tryptophan residue in HSA, buried deep in subdomain IIA where a large hydrophobic cavity exists and small hydrophobic molecules can penetrate and bind. Therefore, the primary binding site of examined Pd–complexes on HSA is likely to be subdomain IIA.

To examine the exact location of binding site on HSA for these two Pd–ligands, the competitive displacement experiments were carried out using warfarin as a characteristic marker for site I at subdomain IIA [91] and ibuprofen for site II at subdomain IIIA. Compared with the association constant of the HSA–Pd-complexes system in the absence of the site marker (Table 1), it was obvious that the value of the K_a decreased significantly with the addition of warfarin ($1.2 \times 10^4\ M^{-1}$ for **1** and $2.9 \times 10^4\ M^{-1}$ for **3**), whereas it remained almost the same with the addition of ibuprofen. The results suggested that Pd-ligands and warfarin share the same binding place on HSA, located in region of subdomain IIA.

Circular dichroism (CD) is a sensitive method to monitor the conformational changes in the protein. The effect of Pd-complexes on HSA conformation was investigated by far-UV CD spectra (Fig. 5C). As expected, the CD spectra of HSA showed two negative bands in the UV region at around 208 and 222 nm, which are characteristic of the α-helix structure of protein. Upon Pd-ligands (**1** or **3**) interaction, there was a minor increase in α-helices content (from 48.1% for free HSA up to 50.3%). Therefore, the conformation of HSA was little affected by the addition of ligands.

Taken together, these results indicate that HSA could be a suitable carrier for transport of examined complexes with strong anticancer activity through systemic circulation.

3.3. Docking of *1* and *3* to HSA

Docking of complexes **1** and **3** to HSA structure 2BXD gave conformations with lowest binding energies −5.34 and −4.79 kcal mol^{-1}, respectively. Complex **1** forms hydrophilic interactions with amino acid residue Arg 222 and hydrophobic interactions with Ile 264, Leu 234, Leu 260, Arg 257, Leu 238, His 242, Val 241 and Tyr 150 (Fig. 6A). Complex **3** forms hydrophilic interactions with amino acid residue Arg 222 and hydrophobic interactions with residues Arg 222, Ala 291, Ile 290, Ile 264, Leu 260, Arg 257, Tyr 150, Leu 238, His 242, Lys 199, Trp 214 (Fig. 6B). Both, **1** and **3** fail to form hydrogen bonds with His 242 and Tyr 150 due to flat structure and incapability to satisfy hydrogen bond angle criteria in line Pd-Cl-H atoms. Docked conformations of both complexes are near to Trp 214, thus explaining fluorescence experiment results. Regarding binding energies, they are consistent with experimental association constants K_a, because lower binding energy of **1** would consider somewhat higher value of association constant, as reported in the experimental part (Supplementary material). Regarding

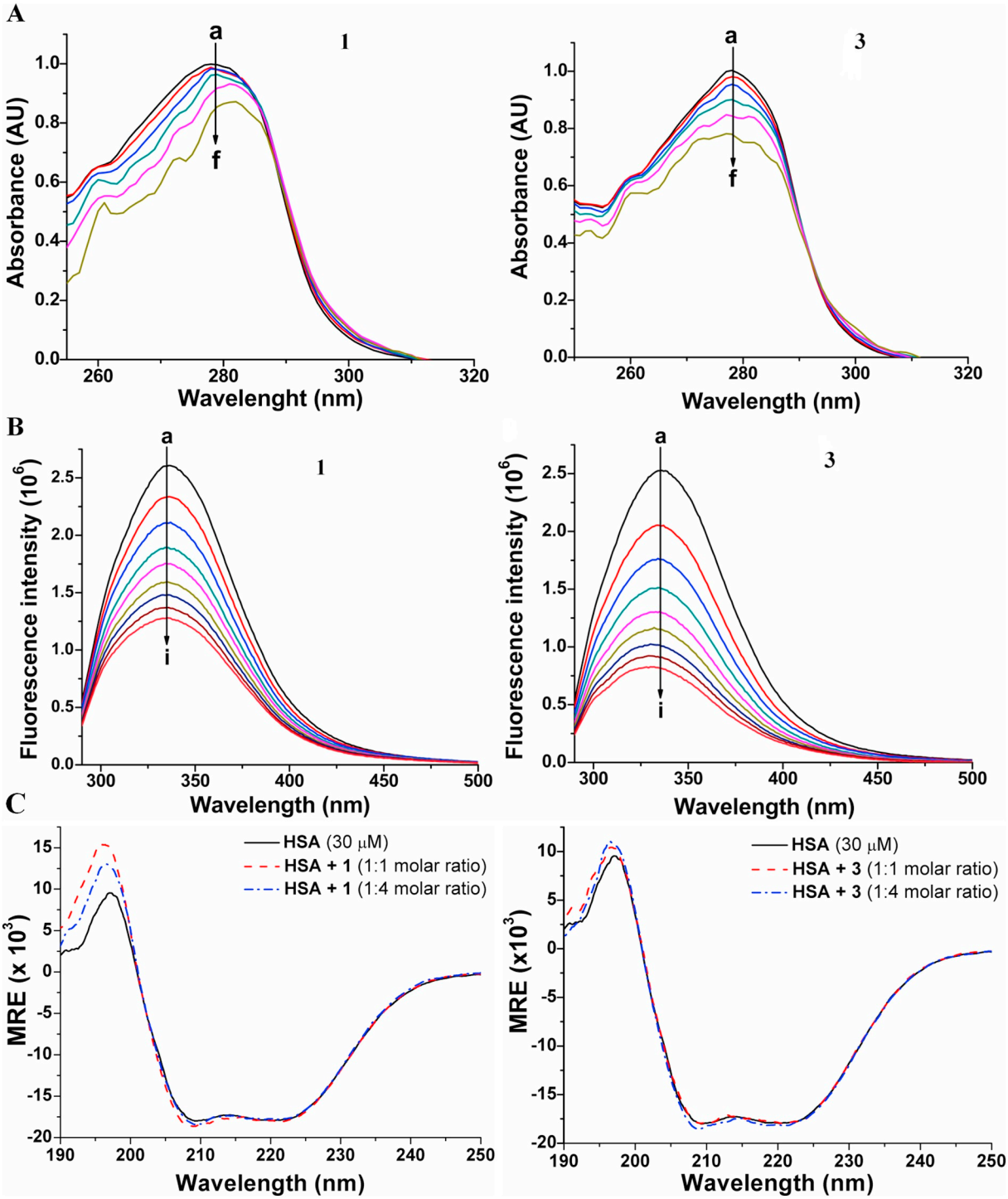

Fig. 5. Monitoring of **1** (left panels) and **3** (right) binding to HSA (at pH 7.4) by spectroscopic methods. (A) UV absorption spectra of 10 μM HSA incubated in the presence of 0, 5, 10, 20, 30 and 40 μM of ligands (curves a to f, respectively); (B) Emission spectra of 1 μM HSA (excitation at 280 nm) in the presence of 0, 2, 4, 6, 8, 10, 12 and 14 μM of ligands (curves a to h, respectively); (C) Effect of **1** or **3** addition on the far UV CD spectra of HSA.

comparison between experimental and calculated binding affinity of warfarin to HSA using this method, we report calculated binding energy of $-5.12\,\text{kcal mol}^{-1}$, and root-mean square deviation (RMSD) of 1.3861 Å with respect to crystal coordinates in PDB structure 2BXD, while experimental binding affinity of warfarin to HSA was found to be 4.6 μM [92] or $-7.26\,\text{kcal mol}^{-1}$. The difference is significant and the relative error 29.47% by means of binding energy, but analogously we can estimate that binding of both complexes is significant but lower than warfarin's. This is in accordance with both theoretical and experimental binding constants of **1** and **3**, because their association constants of $3.2 \times 10^4\,\text{M}^{-1}$ and $2 \times 10^5\,\text{M}^{-1}$ correspond to dissociation constants of 31.25 μM ($\Delta G = -6.13\,\text{kcal mol}^{-1}$) and 5 μM ($\Delta G = -7.22\,\text{kcal mol}^{-1}$). Therefore, calculated binding energies of **1** and **3** are, although in inverted order with respect to experimental values, and considering reported error, in accordance with their order of magnitude (Table 2).

Table 1
The SV quenching constants (K_{SV}), bimolecular quenching constants (k_q), binding constant (K_a) and the number of binding sites (n) on the HSA-Pd complexes system at different temperatures (n = 3).

Complex	t (°C)	K_{SV} (M^{-1}) × 10^{6a}	k_q ($M^{-1}s^{-1}$) × 10^{14a}	K_a (M^{-1}) × 10^{5b}	n^b
3	25	1.16 ± 0.103	1.16	1.59 ± 0.111	0.83 ± 0.02
	30	1.07 ± 0.125	1.07	1.32 ± 0.129	0.85 ± 0.01
	37	1.01 ± 0.085	1.01	1.12 ± 0.092	0.91 ± 0.02
1	25	1.10 ± 0.121	1.10	1.11 ± 0.214	0.89 ± 0.02
	30	1.08 ± 0.099	1.08	1.01 ± 0.105	0.93 ± 0.01
	37	1.06 ± 0.105	1.06	0.89 ± 0.087	0.90 ± 0.02

[a] Calculated according equation S2 (Supplementary material).
[b] Calculated according equation S3 (Supplementary material).

3.4. Docking of **1** and **3** to DNA

Docking of both, **1** and **3**, to both structures of DNA, 4UA8 and 3U2N showed binding to minor groove (Fig. 7), with following lowest binding energies values (Table 2). The orientation of both complexes toward DNA is the same, considering hydrophobic interactions of aromatic systems with nucleotide bases, while Cl atoms are oriented toward exterior space. No stacking interactions were identified. Binding energies suggest low binding affinities to DNA for both complexes, but somewhat stronger than for HSA.

3.5. Docking of **1** and **3** to Topoisomerases

Topoisomerases I and II (Top I and Top II) are both nuclear enzymes which control DNA topology by relaxing its torsional stress. Top I and Top II are involved in many DNA activities, such as RNA synthesis and they manifest their role by relaxing positive and negative torsion by making single (Top I) and double (Top II) transient DNA breaks. Their function also includes relegation of DNA breaks [93]. Inhibition of Top I and Top II, which are overexpressed in solid tumors, results in permanent DNA strand breaks and apoptosis. Because of that, targeting of Top I and Top II is recognized as an effective anticancer strategy and there is a search for novel Topoisomerases inhibitors [8,94]. Investigations on inhibition of Top I and Top II by metal complexes are relatively rare and there are no lead compounds [94,95]. In the case of Pd(II) complexes there are only four experimental [96–100] and one *in silico* [101] study dealing with their Top I [96–98,101] and Top II [99,100] inhibition properties. In order to evaluate inhibition potential of **1** and **3** against Top I and Top II, a docking study has been performed. Due to specific topology of binding sites in both enzymes, it was necessary to optimize partial charges on ligand atoms using the COSMO solvation model in MOPAC 2016. Therefore, we carried redocking of etoplatin from crystal structure 5GWI, iteratively optimizing ligand partial charges until its docking pose converged to the most similar one in crystal structure (Fig. S16, Supplementary material). It was found that pyridine is the best solvent that simulates binding site environment. As binding site of both Topoisomerases is similar, we decided to treat all ligands with this approach.

3.5.1. Docking of **1** and **3** to Top I

Among four downloaded Top I structures, 1T8I, 1SEU, 1SC7 and 1K4T, re-docking of their co-crystallized compounds was shown to be the most reliable (by means of RMSD and binding energy) in the case of 1T8I. The docking of camptothecin into 1T8I gave the lowest energy conformation with RMSD of 0.83 Å in reference to crystal coordinates (Fig. S17, Supplementary material). The obtained ΔG value (Table 2) corresponds to K_d value of the same order of magnitude to experimentally measured IC_{50} value [102]. Therefore, 1T8I was chosen for the docking of both, **1** and **3**. Complexes **1** and **3** are prone to intercalation and form stacking interactions with DNA bases, and similar orientations of acetylcarboxy groups. The calculated binding energies for **1** and **3** are 57.41 and 139.05 μM, respectively. Fig. 8 presents docked conformations of two complexes into Top I. In purpose of additional verification of docking results, seven randomly selected Top I compounds were docked into 1T8I structure and their predicted K_i values were compared with experimental IC_{50} values (Table 3). The linear fit equation is $\ln IC_{50} = 0.5592 \times \ln K_i + 1.7911$ with $R^2 = 0.3332$ ($R = 0.5772$). The lower correlation coefficient is expected because K_i is not directly correlated with IC_{50} values, but its magnitude is enough to justify docking results. Therefore, our results on **1** and **3** predict their micromolar range activity on Top I.

3.5.2. Docking of **1** and **3** to Top II

The RMSD of etoplatin in comparison to crystal coordinates was 2.1013 Å, with reference to heavy atoms. The overlay of corresponding structures is presented in Fig. S16, (Supplementary material). The docked pose of etoplatin shows deviation of Pt atom with reference to

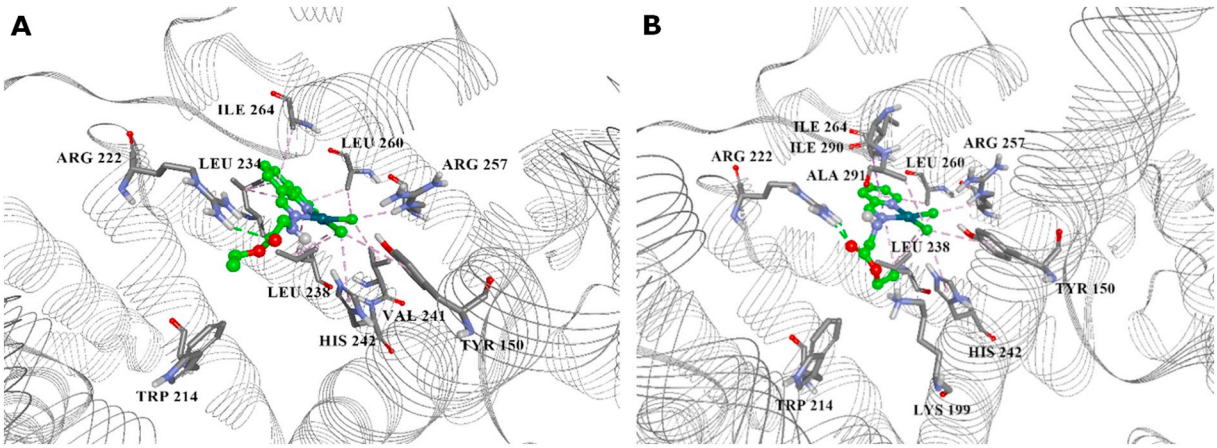

Fig. 6. Complexes **1** (A) and **3** (B) docked into warfarine's binding site of HSA.

Table 2
Experimental (ΔG_e) and calculated (ΔG_c) binding energies (kcal mol^{-1}) to HSA, DNA and Top I and II for investigated and reference compounds.

Compound	ΔG_e HSA	ΔG_c HSA	ΔG_c 3U2N DNA	ΔG_c 4U8A DNA	ΔG_c 1T8I Top I	ΔG_c DNA pocket Top II	ΔG_c Met782 pocket Top II
Warfarine	−7.26	−5.12	–	–	–	–	–
Camptothecin	–	–	–	–	−8.76	–	–
Etoplatin	–	–	–	–	–	–	−6.34
1	−6.13	−5.34	−6.92	−6.87	−5.79	−2.60	−2.94
3	−7.22	−4.79	−5.09	4.79	−5.26	−3.50	−2.57

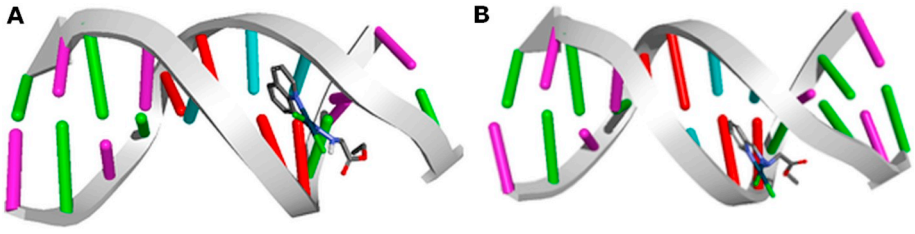

Fig. 7. Complexes **1** (A) and **3** (B) docked into DNA, structure PDB 4U8A/PDB 3U2N.

crystal coordinates, but corresponding interactions with Met 782 are reserved. Both, **1** and **3**, show docked poses in two pockets: one showing intercalation in DNA, other when interacting with Met782. This is understood as etoplatin occupies both, with Pt head oriented toward Met782. The docking poses are presented in Figs. S18–S21, (Supplementary material) while corresponding binding energies for etoplatin and investigated complexes are given in Table 2. The complex **3** is bound to DNA more strongly than **1**. On the other hand, **1** shows greater preference to Met782 pocket both from **3** and its own intercalated pose. Compared to the binding of etoplatin, both **1** and **3** bind much weaker in a millimolar range (Table 2).

Table 3
Referent CHEMBL compounds with docking energies and experimental data.

CHEMBL ID	Calculated binding energy (kcal mol^{-1})/K_i (nM)	Measured IC_{50} value (nM)
CHEMBL84	−8.83/336.78	50
CHEMBL13523	−9.06/227.03	505
CHEMBL93122	−5.65/71,690	1000
CHEMBL163007	−9.40/129.82	200
CHEMBL338843	−8.94/279.20	11
CHEMBL422886	−9.11/211.56	100
CHEMBL3627832	−7.39/3840	10,000

3.6. DNA Top I inhibitory activity of *1* and *3*

The effect of **1** and **3** on changes in the structure of a supercoiled (SC) DNA caused by the activity of Top I was evaluated by their ability to interact with Top I and consequently modify the mobility of the circular pBlueScript SK (−) plasmid in a gel electrophoresis assay. It was observed that **1** and **3** were able to change electrophoretic mobility of circular DNA in a dose dependent manner.

The inhibitory ability of **1** on the activity of Top I has been evaluated in the broad range of concentrations (from 0.1 μM to 1000 μM) (Fig. 9A). The results clearly showed that in tested conditions SC pBlueScript SK (−) plasmid DNA was fully relaxed by the enzyme, while the activity of Top I was completely inhibited at 10 μM concentration of **1**. At higher concentrations of **1** (100, 500 and 1000 μM) it was observed the degradation of DNA. Considering the sudden transition of the relaxed to the SC form of pBlueScript SK (−) plasmid DNA by **1**, the same assay with wider ranges of lower concentrations (from 0.1 μM to 10 μM) was performed. The results showed that by increasing of the concentration of **1** (from 1 μM to 10 μM) the levels of relaxed form of DNA were decreased, and the activity of Top I was completely inhibited at concentration of **1** between 2 and 4 μM (Fig. 9B).

An analysis of the Top I inhibition by **3** was also performed in the same assay. We got very similar results as obtained for **1** in case of testing in the wide range of concentrations (from 0.1 μM to 1000 μM) (Fig. S22A, Supplementary material). A more precise analysis in a wider range of lower concentrations of **3** (0.1, 1, 2, 4, 6, 8 and 10 μM) has shown that the ability of **1** to inhibit the relaxation of DNA was slightly stronger than **3**; the activity of Top I was completely inhibited at 10 μM concentration of **3** (Fig. S22B, Supplementary material) in comparison to the inhibitory concentration of **1** (2–4 μM).

Both of the tested complexes inhibited significantly DNA relaxation in a concentration dependent manner, while the **3** showed slightly

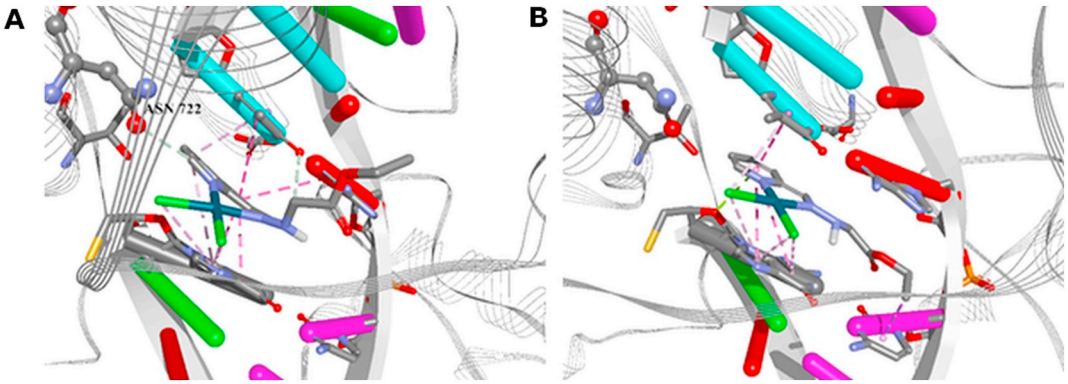

Fig. 8. Complexes **1** (A) and **3** (B) docked into active site of structure 1T8I. Green: hydrophilic interactions. Purple/grey: aromatic and other hydrophobic interactions. (For interpretation of the references to color in this figure legend, the reader is referred to the web version of this article.)

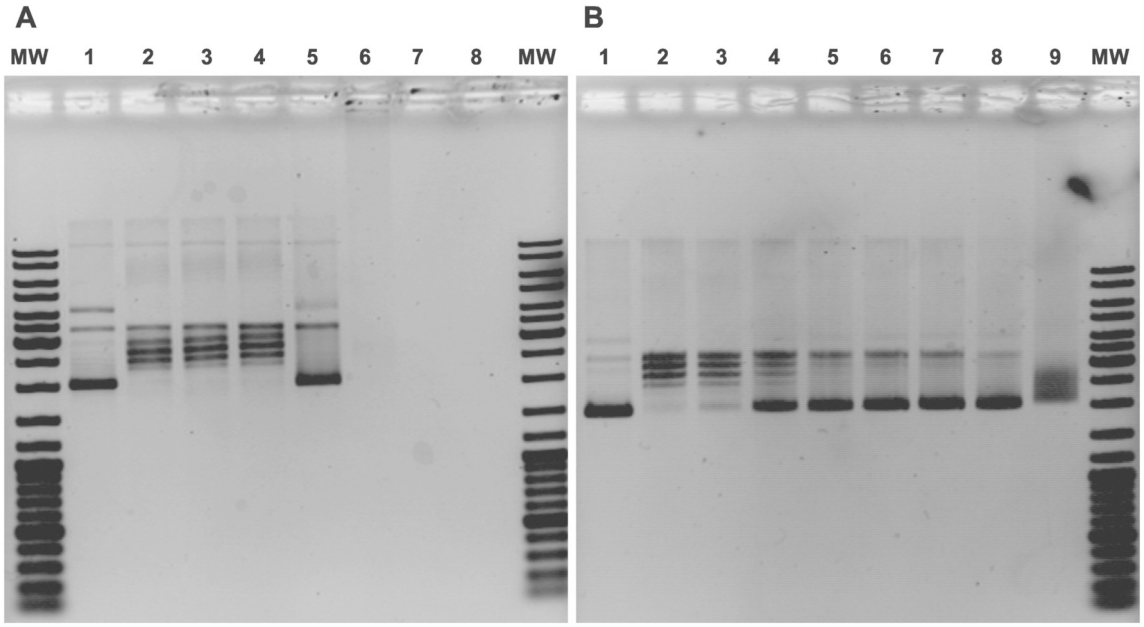

Fig. 9. Agarose gel electrophoresis picture showing Top I inhibition by increasing concentrations of **1**. Lanes: (A and B - MW) Gene Ruler DNA Ladder Mix 0.1–10 kb (ThermoFisherScientific); (A and B - 1) pBlueScript SK (−) without Top I; (A and B - 2) pBlueScript SK (−) with Top I; (A 3–8 and B 3–9) pBlueScript SK (−) with Top I and increasing concentrations of **1**: (A3) 0.1 μM; (A4) 1 μM; (A5) 10 μM; (A6) 100 μM; (A7) 500 μM; (A8) 1000 μM; (B3) 1 μM; (B4) 2 μM; (B5) 4 μM; (B6) 6 μM; (B7) 8 μM; (B8) 10 μM; (B9) 25 μM.

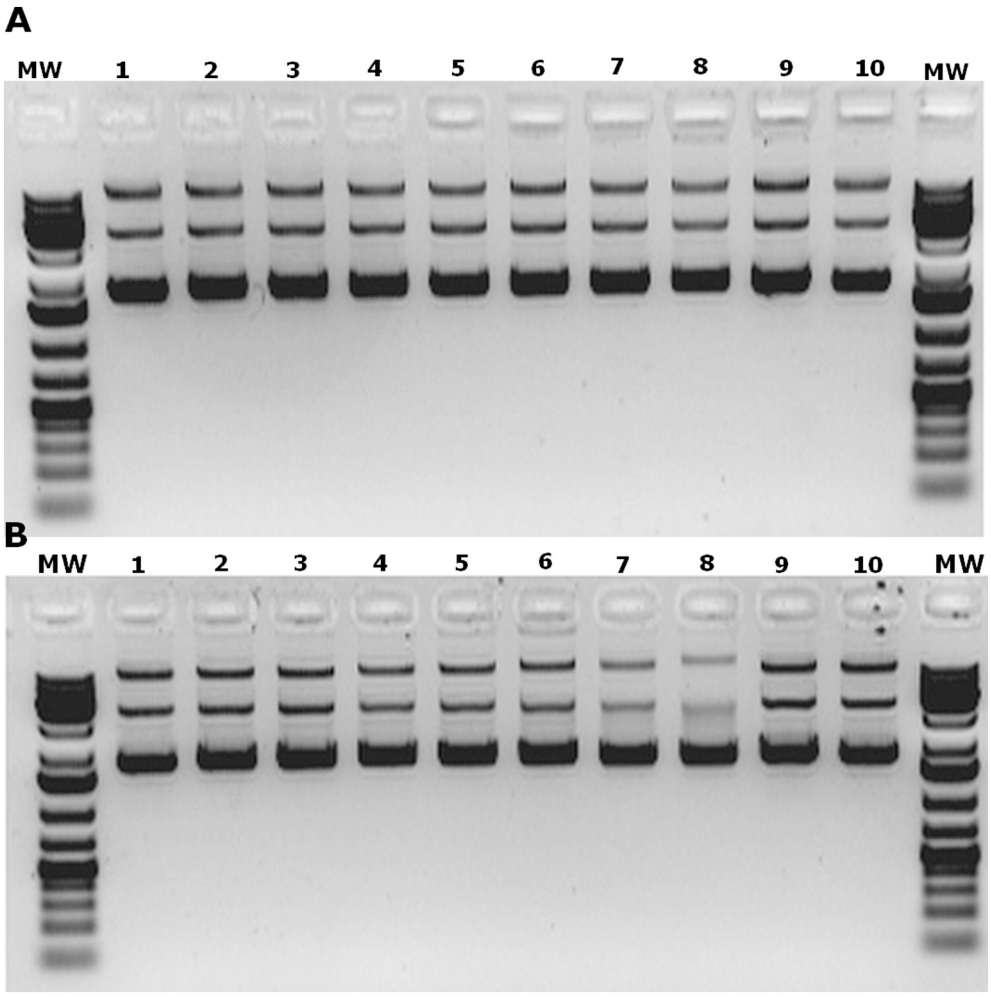

Fig. 10. Results of agarose gel electrophoresis of interaction of pBlueScript SK (−) plasmid with **1** (A) and 3 (B) after 90 min of incubation. Lane 1 – control plasmid pBlueScript SK (−); lane 2, 3, 4, 5, 6, 7 and 8 – plasmid pBlueScript SK (−) with 50 μM, 100 μM, 200 μM, 300 μM, 500 μM, 750 μM and 1000 μM of corresponding the complex; lane 9 – control plasmid pBlueScript SK (−) + 3 μM of DMSO; Lane 10 – control plasmid pBlueScript SK (−); MW - Gene Ruler DNA Ladder Mix 0.1–10 kb (ThermoFisherScientific).

lower effect (**1** completely inhibited Top I activity at concentration of 3 μM, while the concentration of 10 μM of **3** was necessary for complete inhibition of Top I activity). Similar results were obtained by the other authors [96,98].

3.7. Gel electrophoresis study of interactions of *1* and *3* with plasmid DNA

The interaction of **1** and **3** with plasmid DNA was monitored by agarose gel electrophoresis in order to evaluate their nuclease activity and propensity to covalent binding. In the case of nuclease activity, transformation of untreated plasmid SC form in nicked (N) and linear (L) forms is an indicator of nuclease activity, while retardation of SC form indicates covalent binding of investigated complexes to plasmid DNA [103].

We investigated the effect of **1** and **3** on pBlueScript SK (−) plasmid in 5 mM Tris buffer (pH = 7.2) within two incubation times (90 and 120 min) in the range of applied concentrations (50–1000 μM). As it is shown in Fig. 10 (lane 2, top), pBlueScript SK (−) plasmid consists mainly of SC form, while presence of other two forms have been also noticed. Our results indicate that there is no nuclease activity or covalent binding of investigated complexes on plasmid DNA after 90 min of incubation (Fig. 10). Nuclease activity of both, **1** and **3**, was detected after 120 min of incubation, based on the changes in intensities of different DNA forms (Fig. S23, Supplementary material). Nuclease activity of **1** at 1000 μM was detected since N and L forms disappeared (lane 8, top), while in the case of **3** diminishing of N and disappearance of L form in at 750 μM was observed (lane 7, bottom). Obtained nuclease activities of **1** and **3** at high micromolar concentrations, indicate that nuclease activity cannot be considered as mechanism of action of investigated complexes under physiological conditions, since their AD_{50} values were in the low micromolar range.

4. Conclusions

Anticancer activity of five Pd(II) complexes with *N*-heteroaromatic hydrazones against THP-1 and MCF-7 cell lines was studied. Since **1** and **3** induced apoptosis in investigated cell lines they were selected for further biological studies. Our data revealed that ROS production is partly responsible for mechanism of anticancer activity of **1** and **3**, while changes in cell cycle distribution indicate that both complexes interfered with DNA replication process. The combination of experimental and *in silico* studies indicated that **1** and **3** cause a DNA damage directly by binding to the minor groove and indirectly by Top I inhibition. Our results indicated that Pd(II) complexes with bidentate *N*-heteroaromatic hydrazone ligands represent a promising scaffold for design of novel DNA damaging agents which target DNA directly and indirectly. Our further investigation will be focused on experimental work in order to confirm multi-targeting hypothesis and to obtain more potent derivatives.

Abbreviations

MBC	metal-based chemotherapeutic
haOEt × HCl	ethyl hydrazinoacetate hydrochloride
q8a	quinoline-8-carboxaldehyde
q2a	quinoline-2-carboxaldehyde
py2a	2-formylpyridine
py2ac	2-acetylpyridine
py2bz	2-benzoylpyridine
HL60	human promyelocytic leukemia
U251	human glioma
C6	rat glioma
L929	mouse fibrosarcoma
Bcl-2	B-cell lymphoma 2
MTT	3-(4,5-dimethylthiazol-2-yl)-2,5-diphenyltetrazolium bromide
MCF-7	human mammary adenocarcinoma cell line
THP-1	acute monocytic leukemia cell line
Annexin V	Ca^{2+}- dependent phospholipid-binding protein with high affinity for phosphatidylserine
PI	propidium iodide
HSA	human serum albumin
Top I	topoisomerase I
Top II	topoisomerase II
Bid	BH3 interacting-domain death agonist
ROS	reactive oxygen species
PTPs	mitochondrial permeability transition pores
$O_2\cdot^-$	superoxide anion radical
MTP	mitochondrial transmembrane potential
mtDNA	mitochondrial DNA
NER	nucleotide excision repair (pathway)
SOD	superoxide dismutase
MDA-MB-231	human breast cancer cell line
MCF-10A	human mammary epithelial cell line
MFI	median fluorescent intensity
AU	arbitrary units
mPTP	mitochondrial permeability transition pore
2D	two-dimensional
3D	three-dimensional
SV	Stern-Volmer (equation)
CD	circular dichroism
ATR	Attenuated Total Reflection
ER	endoplasmatic reticulum
7-AAD	7-aminoactinomycin D
SOD1	copper/zinc superoxide dismutase
SOD2	manganese superoxide dismutase
dMTP	dissipated mitochondrial transmembrane potential
IIA	Sudlon's site I
IIIA	Sudlon's site II
N	nicked (DNA)
L	linear (DNA)
SC	supercoiled (DNA)
RMSD	root-mean square deviation

Acknowledgements

The Ministry of Education, Science and Technological Development of the Republic of Serbia under Grant 172055 financially supported this work. This Article is based upon work from COST Actions CA15135 and CA16119 supported by COST.

Appendix A. Supplementary data

Supplementary data to this article can be found online at https://doi.org/10.1016/j.jinorgbio.2019.110758.

References

[1] M. Naghavi, A.A. Abajobir, C. Abbafati, K.M. Abbas, F. Abd-Allah, S.F. Abera, V. Aboyans, et al., Global, regional, and national age-sex specific mortality for 264 causes of death, 1980–2016: a systematic analysis for the Global Burden of Disease Study 2016, Lancet 390 (2017) 1151–1210, https://doi.org/10.1016/S0140-6736(17)32152-9.
[2] T. Helleday, E. Petermann, C. Lundin, B. Hodgson, R.A. Sharma, DNA repair pathways as targets for cancer therapy, Nat. Rev. Cancer 8 (2008) 193–204, https://doi.org/10.1038/nrc2342.
[3] L.H. Swift, R.M. Golsteyn, Genotoxic anti-cancer agents and their relationship to DNA damage, mitosis, and checkpoint adaptation in proliferating cancer cells, Int. J. Mol. Sci. 15 (2014) 3403–3431, https://doi.org/10.3390/ijms15033403.
[4] M. Fojta, A. Daňhel, L. Havran, V. Vyskočil, Recent progress in electrochemical sensors and assays for DNA damage and repair, TrAC - Trends Anal. Chem. 79 (2016) 160–167, https://doi.org/10.1016/j.trac.2015.11.018.
[5] V. Bianchi, E. Pontis, P. Reichard, Changes of deoxyribonucleoside triphosphate pools induced by hydroxyurea and their relation to DNA synthesis, J. Biol. Chem. 261 (1986) 16037–16042.
[6] S. Ikegami, T. Taguchi, M. Ohashi, M. Oguro, H. Nagano, Y. Mano, Aphidicolin prevents mitotic cell division by interfering with the activity of DNA polymerase-

α, Nature 275 (1978) 458–460, https://doi.org/10.1038/275458a0.
[7] Y. Pommier, J.M. Barcelo, V.A. Rao, O. Sordet, A.G. Jobson, L. Thibaut, Z.-H. Miao, J.A. Seiler, H. Zhang, C. Marchand, K. Agama, J.L. Nitiss, C. Redon, Repair of topoisomerase I-mediated DNA damage, Prog. Nucleic Acid Res. Mol. Biol. 81 (2006) 179–229, https://doi.org/10.1016/S0079-6603(06)81005-6.
[8] J.L. Nitiss, Targeting DNA topoisomerase II in cancer chemotherapy, Nat. Rev. Cancer 9 (2009) 338–350, https://doi.org/10.1038/nrc2607.
[9] N.P.E. Barry, P.J. Sadler, Exploration of the medical periodic table: towards new targets, Chem. Commun. 49 (2013) 5106–5131, https://doi.org/10.1039/c3cc41143e.
[10] A.M. Havelka, M. Berndtsson, M.H. Olofsson, M.C. Shoshan, S. Linder, Mechanisms of action of DNA-damaging anticancer drugs in treatment of carcinomas: is acute apoptosis an "off-target" effect? Mini Rev. Med. Chem. 7 (2007) 1035–1039, https://doi.org/10.2174/138955707782110196.
[11] D.M. Cheff, M.D. Hall, A drug of such damned nature. 1 Challenges and opportunities in translational platinum drug research, J. Med. Chem. 60 (2017) 4517–4532, https://doi.org/10.1021/acs.jmedchem.6b01351.
[12] S. Dasari, P. Bernard Tchounwou, Cisplatin in cancer therapy: molecular mechanisms of action, Eur. J. Pharmacol. 740 (2014) 364–378, https://doi.org/10.1016/j.ejphar.2014.07.025.
[13] N.J. Wheate, S. Walker, G.E. Craig, R. Oun, The status of platinum anticancer drugs in the clinic and in clinical trials, Dalton Trans. 39 (2010) 8113–8127, https://doi.org/10.1039/c0dt00292e.
[14] T.C. Johnstone, K. Suntharalingam, S.J. Lippard, The next generation of platinum drugs: targeted Pt(II) agents, nanoparticle delivery, and Pt(IV) prodrugs, Chem. Rev. 116 (2016) 3436–3486, https://doi.org/10.1021/acs.chemrev.5b00597.
[15] M.N. Alam, F. Huq, Comprehensive review on tumour active palladium compounds and structure–activity relationships, Coord. Chem. Rev. 316 (2016) 36–67, https://doi.org/10.1016/J.CCR.2016.02.001.
[16] S. Medici, M. Peana, V.M. Nurchi, J.I. Lachowicz, G. Crisponi, M.A. Zoroddu, Noble metals in medicine: latest advances, Coord. Chem. Rev. 284 (2015) 329–350, https://doi.org/10.1016/j.ccr.2014.08.002.
[17] A.R. Kapdi, I.J.S. Fairlamb, Anti-cancer palladium complexes: a focus on PdX_2L_2, palladacycles and related complexes, Chem. Soc. Rev. 43 (2014) 4751–4777, https://doi.org/10.1039/C4CS00063C.
[18] M. Fanelli, M. Formica, V. Fusi, L. Giorgi, M. Micheloni, P. Paoli, New trends in platinum and palladium complexes as antineoplastic agents, Coord. Chem. Rev. 310 (2016) 41–79, https://doi.org/10.1016/j.ccr.2015.11.004.
[19] N. Filipović, S. Grubišić, M. Jovanović, M. Dulović, I. Marković, O. Klisurić, A. Marinković, D. Mitić, K. Anđelković, T. Todorović, Palladium(II) complexes with N-heteroaromatic bidentate hydrazone ligands: the effect of the chelate ring size and lipophilicity on in vitro cytotoxic activity, Chem. Biol. Drug Des. 84 (2014) 333–341, https://doi.org/10.1111/cbdd.12322.
[20] M.-X. Li, C.-L. Chen, C.-S. Ling, J. Zhou, B.-S. Ji, Y.-J. Wu, J.-Y. Niu, Cytotoxicity and structure–activity relationships of four α-N-heterocyclic thiosemicarbazone derivatives crystal structure of 2-acetylpyrazine thiosemicarbazone, Bioorg. Med. Chem. Lett. 19 (2009) 2704–2706, https://doi.org/10.1016/J.BMCL.2009.03.135.
[21] J. Easmon, G. Pürstinger, K.-S. Thies, G. Heinisch, J. Hofmann, Synthesis, structure – activity relationships, and antitumor studies of 2-benzoxazolyl hydrazones derived from alpha-(N)-acyl heteroaromatics, J. Med. Chem. 49 (2006) 6343–6350, https://doi.org/10.1021/JM060232U.
[22] K.S.O. Ferraz, L. Ferandes, D. Carrilho, M.C.X. Pinto, M. de F. Leite, E.M. Souza-Fagundes, N.L. Speziali, I.C. Mendes, H. Beraldo, 2-Benzoylpyridine-N(4)-tolyl thiosemicarbazones and their palladium(II) complexes: cytotoxicity against leukemia cells, Bioorg. Med. Chem. 17 (2009) 7138–7144, https://doi.org/10.1016/J.BMC.2009.08.063.
[23] C. Stefani, P.J. Jansson, E. Gutierrez, P.V. Bernhardt, D.R. Richardson, D.S. Kalinowski, Alkyl substituted 2′-benzoylpyridine thiosemicarbazone chelators with potent and selective anti-neoplastic activity: novel ligands that limit methemoglobin formation, J. Med. Chem. 56 (2013) 357–370, https://doi.org/10.1021/jm301691s.
[24] J.K. Park, Y.M. Chung, B.-G. Kim, Y.-A. Yoo, B.-S. Yang, J.S. Kim, Y. Do Yoo, N'-(phenyl-pyridin-2-yl-methylene)-hydrazine carbodithioic acid methyl ester enhances radiation-induced cell death by targeting Bcl-2 against human lung carcinoma cells, Mol. Cancer Ther. 3 (2004) 403–407.
[25] B. Cascella, S.G. Lee, S. Singh, J.M. Jez, L.M. Mirica, The small molecule JIB-04 disrupts O_2 binding in the Fe-dependent histone demethylase KDM4A/JMJD2A, Chem. Commun. 53 (2017) 2174–2177, https://doi.org/10.1039/C6CC09882G.
[26] J. Easmon, G. Heinisch, G. Pürstinger, T. Langer, J.K. Österreicher, H.H. Gruniche, J. Hofmann, Azinyl and diazinyl hydrazones derived from aryl N-heteroaryl ketones: synthesis and antiproliferative activity, J. Med. Chem. 40 (1997) 4420–4425, https://doi.org/10.1021/JM970255W.
[27] Y. Yu, Y. Suryo Rahmanto, C.L. Hawkins, D.R. Richardson, The potent and novel thiosemicarbazone chelators di-2-pyridylketone-4,4-dimethyl-3-thiosemicarbazone and 2-benzoylpyridine-4,4-dimethyl-3-thiosemicarbazone affect crucial thiol systems required for ribonucleotide reductase activity, Mol. Pharmacol. 79 (2011) 921–931, https://doi.org/10.1124/mol.111.071324.
[28] K.O.S. Ferraz, G.M.M. Cardoso, C.M. Bertollo, E.M. Souza-Fagundes, N. Speziali, C.L. Zani, I.C. Mendes, M.A. Gomes, H. Beraldo, N(4)-tolyl-2-benzoylpyridine-derived thiosemicarbazones and their palladium(II) and platinum(II) complexes: cytotoxicity against human solid tumor cells, Polyhedron 30 (2011) 315–321, https://doi.org/10.1016/J.POLY.2010.10.014.
[29] H. Wu, X. Sun, Y. Lu, X. Fang, M. Li, Palladium(II) and antimony(III) complexes derived from 2-benzoylpyridine N^4-phenylthiosemicarbazone: synthesis, crystal structure, antiproliferative activity, and low toxicity on normal hepatocyte QSG7701 cells, Synth. React. Inorganic, Met. Nano-Metal Chem. 45 (2015) 1859–1863, https://doi.org/10.1080/15533174.2013.865230.
[30] S.P. Manandhar, E.R. Hildebrandt, W.K. Schmidt, Small-molecule inhibitors of the Rce1p CaaX protease, J. Biomol. Screen. 12 (2007) 983–993, https://doi.org/10.1177/1087057107307226.
[31] Oxford Diffraction CrysAlis CCD and CrysAlis Red, Oxford Diffraction, 2009.
[32] M.C. Burla, R. Caliandro, B. Carrozzini, G.L. Cascarano, C. Cuocci, C. Giacovazzo, M. Mallamo, A. Mazzone, G. Polidori, Crystal structure determination and refinement via SIR2014, J. Appl. Crystallogr. 48 (2015) 306–309, https://doi.org/10.1107/S1600576715001132.
[33] G.M. Sheldrick, SHELX97: Program for the Refinement of Crystal Structures, (1997).
[34] L.J. Farrugia, ORTEP-3 for Windows, (1997).
[35] C.F. Macrae, I.J. Bruno, J.A. Chisholm, P.R. Edgington, P. McCabe, E. Pidcock, L. Rodriguez-Monge, R. Taylor, J. van de Streek, P.A. Wood, Mercury CSD 2.0 - new features for the visualization and investigation of crystal structures, J. Appl. Crystallogr. 41 (2008) 466–470, https://doi.org/10.1107/S0021889807067908.
[36] L.J. Farrugia, IUCr, *WinGX* suite for small-molecule single-crystal crystallography, J. Appl. Crystallogr. 32 (1999) 837–838, https://doi.org/10.1107/S0021889899006020.
[37] A.L. Spek, Structure validation in chemical crystallography, Acta Crystallogr. Sect. D Biol. Crystallogr. 65 (2009) 148–155, https://doi.org/10.1107/S090744490804362X.
[38] Ş. Comşa, A.M. Cîmpean, M. Raica, The story of MCF-7 breast cancer cell line: 40 years of experience in research, Anticancer Res. 35 (2015) 3147–3154.
[39] P.B. Gupta, C.M. Fillmore, G. Jiang, S.D. Shapira, K. Tao, C. Kuperwasser, E.S. Lander, Stochastic state transitions give rise to phenotypic equilibrium in populations of cancer cells, Cell 146 (2011) 633–644, https://doi.org/10.1016/j.cell.2011.07.026.
[40] N.R. Filipović, S. Bjelogrlić, A. Marinković, T. Verbic, I.N. Cvijetić, M. Senćanski, M.V. Rodić, M. Vujčić, D. Sladić, Z. Striković, T.R. Todorović, C.D. Muller, Zn(II) complex with 2-quinolinecarboxaldehyde selenosemicarbazone: synthesis, structure, interaction studies with DNA/HSA, molecular docking and caspase-8 and -9 independent apoptose induction, RSC Adv. (2015) 95191–95211, https://doi.org/10.1039/C5RA19849F.
[41] J.M. Wagner, L.M. Karnitz, Cisplatin-induced DNA damage activates replication checkpoint signaling components that differentially affect tumor cell survival, Mol. Pharmacol. 76 (2009) 208–214, https://doi.org/10.1124/mol.109.055178.
[42] C.W. Yde, O.G. Issinger, Enhancing cisplatin sensitivity in MCF-7 human breast cancer cells by down-regulation of Bcl-2 and cyclin D1, Int. J. Oncol. 29 (2006) 1397–1404, https://doi.org/10.3892/ijo.29.6.1397.
[43] L.Y. Lim, N. Vidnovic, L.W. Ellisen, C.-O. Leong, Mutant p53 mediates survival of breast cancer cells, Br. J. Cancer 101 (2009) 1606–1612, https://doi.org/10.1038/sj.bjc.6605335.
[44] S. Durland-Busbice, D. Reisman, Lack of p53 expression in human myeloid leukemias is not due to mutations in transcriptional regulatory regions of the gene, Leukemia 16 (2002) 2165–2167, https://doi.org/10.1038/sj.leu.2402647.
[45] L.D. Attardi, A. de Vries, T. Jacks, Activation of the p53-dependent G1 checkpoint response in mouse embryo fibroblasts depends on the specific DNA damage inducer, Oncogene 23 (2004) 973–980, https://doi.org/10.1038/sj.onc.1207026.
[46] M. Lupi, G. Matera, C. Natoli, V. Colombo, P. Ubezio, The contribution of p53 in the dynamics of cell cycle response to DNA damage interpreted by a mathematical model, Cell Cycle 6 (2007) 943–950, https://doi.org/10.4161/cc.6.8.4103.
[47] J.-H. Jeong, S.-S. Kang, K.-K. Park, H.-W. Chang, J. Magae, Y.-C. Chang, p53-independent induction of G1 arrest and p21WAF1/CIP1 expression by ascofuranone, an isoprenoid antibiotic, through downregulation of c-Myc, Mol. Cancer Ther. 9 (2010) 2102–2113, https://doi.org/10.1158/1535-7163.MCT-09-1159.
[48] D.R. McIlwain, T. Berger, T.W. Mak, Caspase functions in cell death and disease, Cold Spring Harb. Perspect. Biol. 5 (2013), https://doi.org/10.1101/cshperspect.a008656 (a008656–a008656).
[49] A. Ashkenazi, Targeting death and decoy receptors of the tumour-necrosis factor superfamily, Nat. Rev. Cancer 2 (2002) 420–430, https://doi.org/10.1038/nrc821.
[50] J. da Silva Correia, Y. Miranda, N. Leonard, J. Hsu, R.J. Ulevitch, Regulation of Nod1-mediated signaling pathways, Cell Death Differ. 14 (2007) 830–839, https://doi.org/10.1038/sj.cdd.4402070.
[51] Z. Mahmood, Y. Shukla, Death receptors: targets for cancer therapy, Exp. Cell Res. 316 (2010) 887–899, https://doi.org/10.1016/j.yexcr.2009.12.011.
[52] A. Jimbo, E. Fujita, Y. Kouroku, J. Ohnishi, N. Inohara, K. Kuida, K. Sakamaki, S. Yonehara, T. Momoi, ER stress induces caspase-8 activation, stimulating cytochrome c release and caspase-9 activation, Exp. Cell Res. 283 (2003) 156–166, https://doi.org/10.1016/S0014-4827(02)00033-2.
[53] J. Puccini, L. Dorstyn, S. Kumar, Caspase-2 as a tumour suppressor, Cell Death Differ. 20 (2013) 1133–1139, https://doi.org/10.1038/cdd.2013.87.
[54] L. Bouchier-Hayes, D.R. Green, Caspase-2: the orphan caspase, Cell Death Differ. 19 (2012) 51–57, https://doi.org/10.1038/cdd.2011.157.
[55] C. Bonzon, L. Bouchier-Hayes, L.J. Pagliari, D.R. Green, D.D. Newmeyer, Caspase-2-induced apoptosis requires bid cleavage: a physiological role for bid in heat shock-induced death, Mol. Biol. Cell 17 (2006) 2150–2157, https://doi.org/10.1091/mbc.E05-12-1107.
[56] L.L. Fava, F.J. Bock, S. Geley, A. Villunger, Caspase-2 at a glance, J. Cell Sci. 125 (2012) 5911–5915, https://doi.org/10.1242/jcs.115105.
[57] H.H. Kim, C.S. Park, Lipotropes regulate BCL-2 gene expression in the human breast cancer cell line, MCF-7, Vitr. Cell. Dev. Biol. - Anim. 38 (2002) 205–207, https://doi.org/10.1290/1071-2690(2002)038<0205:LRBGEI>2.0.CO;2.
[58] B. Majumder, K.W.J. Wahle, S. Moir, A. Schofield, S.-N. Choe, A. Farquharson, I. Grant, S.D. Heys, Conjugated linoleic acids (CLAs) regulate the expression of key apoptotic genes in human breast cancer cells, FASEB J. 16 (2002) 1447–1449, https://doi.org/10.1096/fj.01-0720fje.
[59] M. Marloye, G. Berger, M. Gelbcke, F. Dufrasne, A survey of the mechanisms of action of anticancer transition metal complexes, Future Med. Chem. 8 (2016) 2263–2286, https://doi.org/10.4155/fmc-2016-0153.
[60] M.-J. Hosseini, I. Jafarian, S. Farahani, R. Khodadadi, S.H. Tagavi, P. Naserzadeh, A. Mohammadi-Bardbori, N. Arghavanifard, New mechanistic approach of

inorganic palladium toxicity: impairment in mitochondrial electron transfer, Metallomics 8 (2016) 252–259, https://doi.org/10.1039/c5mt00249d.
[61] F. Shaki, M.-J. Hosseini, M. Ghazi-Khansari, J. Pourahmad, Depleted uranium induces disruption of energy homeostasis and oxidative stress in isolated rat brain mitochondria, Metallomics 5 (2013) 736–744, https://doi.org/10.1039/c3mt00019b.
[62] G. Gasser, I. Ott, N. Metzler-Nolte, Organometallic anticancer compounds, J. Med. Chem. 54 (2011) 3–25, https://doi.org/10.1021/jm100020w.
[63] O.A. Olivero, P.K. Chang, D.M. Lopez-Larraza, M.C. Semino-Mora, M.C. Poirier, Preferential formation and decreased removal of cisplatin-DNA adducts in Chinese hamster ovary cell mitochondrial DNA as compared to nuclear DNA, Mutat. Res. 391 (1997) 79–86, https://doi.org/10.1016/S0165-1218(97)00037-2.
[64] Z. Yang, L.M. Schumaker, M.J. Egorin, E.G. Zuhowski, Z. Guo, K.J. Cullen, Cisplatin preferentially binds mitochondrial DNA and voltage-dependent anion channel protein in the mitochondrial membrane of head and neck squamous cell carcinoma: possible role in apoptosis, Clin. Cancer Res. 12 (2006) 5817–5825, https://doi.org/10.1158/1078-0432.CCR-06-1037.
[65] R. Marullo, E. Werner, N. Degtyareva, B. Moore, G. Altavilla, S.S. Ramalingam, P.W. Doetsch, Cisplatin induces a mitochondrial-ROS response that contributes to cytotoxicity depending on mitochondrial redox status and bioenergetic functions, PLoS One 8 (2013) e81162, , https://doi.org/10.1371/journal.pone.0081162.
[66] P. Xiong, Y. Li, Y. Tang, H. Chen, Proteomic analyses of Sirt1-mediated cisplatin resistance in OSCC cell line, Protein J. 30 (2011) 499–508, https://doi.org/10.1007/s10930-011-9354-9.
[67] T.-C. Hour, Y.-L. Lai, C.-I. Kuan, C.-K. Chou, J.-M. Wang, H.-Y. Tu, H.-T. Hu, C.-S. Lin, W.-J. Wu, Y.-S. Pu, E. Sterneck, A.-M. Huang, Transcriptional up-regulation of SOD1 by CEBPD: a potential target for cisplatin resistant human urothelial carcinoma cells, Biochem. Pharmacol. 80 (2010) 325–334, https://doi.org/10.1016/j.bcp.2010.04.007.
[68] D.P.G. Brown, H. Chin-Sinex, B. Nie, M.S. Mendonca, M. Wang, Targeting superoxide dismutase 1 to overcome cisplatin resistance in human ovarian cancer, Cancer Chemother. Pharmacol. 63 (2009) 723–730, https://doi.org/10.1007/s00280-008-0791-x.
[69] M.P. Murphy, How mitochondria produce reactive oxygen species, Biochem. J. 417 (2009) 1–13, https://doi.org/10.1042/BJ20081386.
[70] T. Fukai, M. Ushio-Fukai, Superoxide dismutases: role in redox signaling, vascular function, and diseases, Antioxid. Redox Signal. 15 (2011) 1583–1606, https://doi.org/10.1089/ars.2011.3999.
[71] L. Papa, M. Hahn, E.L. Marsh, B.S. Evans, D. Germain, SOD2 to SOD1 switch in breast cancer, J. Biol. Chem. 289 (2014) 5412–5416, https://doi.org/10.1074/jbc.C113.526475.
[72] S. Andrzejewski, S.-P. Gravel, M. Pollak, J. St-Pierre, Metformin directly acts on mitochondria to alter cellular bioenergetics, Cancer Metab. 2 (2014) 1–14, https://doi.org/10.1186/2049-3002-2-12.
[73] F. Fontanesi, Mitochondria: Structure and Role in Respiration, eLS, John Wiley & Sons, Ltd, Chichester, UK, 2015, pp. 1–13, https://doi.org/10.1002/9780470015902.a0001380.pub2.
[74] V.P. Skulachev, Bioenergetic aspects of apoptosis, necrosis and mitoptosis, Apoptosis 11 (2006) 473–485, https://doi.org/10.1007/s10495-006-5881-9.
[75] D. Han, E. Williams, E. Cadenas, Mitochondrial respiratory chain-dependent generation of superoxide anion and its release into the intermembrane space, Biochem. J. 353 (2001) 411–416.
[76] M. Crompton, The mitochondrial permeability transition pore and its role in cell death, Biochem. J. 34 (1999) 233–249.
[77] V. Adam-Vizi, A.A. Starkov, Calcium and mitochondrial reactive oxygen species generation: how to read the facts, J. Alzheimers Dis. 20 (2010) S413–S426, https://doi.org/10.3233/JAD-2010-100465.
[78] M. Zoratti, I. Szabò, The mitochondrial permeability transition, Biochim. Biophys. Acta 1241 (1995) 139–176, https://doi.org/10.1016/0304-4157(95)00003-A.
[79] G. Kroemer, L. Galluzzi, C. Brenner, Mitochondrial membrane permeabilization in cell death, Physiol. Rev. 87 (2007) 99–163, https://doi.org/10.1152/physrev.00013.2006.
[80] S. Breslin, L. O'Driscoll, Three-dimensional cell culture: the missing link in drug discovery, Drug Discov. Today 18 (2013) 240–249, https://doi.org/10.1016/j.drudis.2012.10.003.
[81] R. Edmondson, J.J. Broglie, A.F. Adcock, L. Yang, Three-dimensional cell culture systems and their applications in drug discovery and cell-based biosensors, Assay Drug Dev. Technol. 12 (2014) 207–218, https://doi.org/10.1089/adt.2014.573.
[82] H. Baharvand, S.M. Hashemi, S. Kazemi Ashtiani, A. Farrokhi, Differentiation of human embryonic stem cells into hepatocytes in 2D and 3D culture systems in vitro, Int. J. Dev. Biol. 50 (2006) 645–652, https://doi.org/10.1387/ijdb.052072hb.
[83] C.M. Nelson, M.J. Bissell, Modeling dynamic reciprocity: engineering three-dimensional culture models of breast architecture, function, and neoplastic transformation, Semin. Cancer Biol. 15 (2005) 342–352, https://doi.org/10.1016/j.semcancer.2005.05.001.
[84] B.A. Justice, N.A. Badr, R.A. Felder, 3D cell culture opens new dimensions in cell-based assays, Drug Discov. Today 14 (2009) 102–107, https://doi.org/10.1016/j.drudis.2008.11.006.
[85] J. Bin Kim, Three-dimensional tissue culture models in cancer biology, Semin. Cancer Biol. 15 (2005) 365–377, https://doi.org/10.1016/j.semcancer.2005.05.002.
[86] H. Elshaflu, S. Bjelogrlić, C.D. Muller, T.R. Todorović, M. Rodić, A. Marinković, N.R. Filipović, Co(III) complex with (*E*)-2-(2-(pyridine-2-ylmethylene)hydrazinyl)-4-(4-tolyl)-1,3-thiazole: structure and activity against 2-D and 3-D cancer cell models, J. Coord. Chem. 69 (2016) 3354–3366, https://doi.org/10.1080/00958972.2016.1232404.
[87] M. Fasano, S. Curry, E. Terreno, M. Galliano, G. Fanali, P. Narciso, S. Notari, P. Ascenzi, The extraordinary ligand binding properties of human serum albumin, IUBMB Life 57 (2005) 787–796, https://doi.org/10.1080/15216540500404093.
[88] Y. Wang, X. Wang, J. Wang, Y. Zhao, W. He, Z. Guo, Noncovalent interactions between a trinuclear monofunctional platinum complex and human serum albumin, Inorg. Chem. 50 (2011) 12661–12668, https://doi.org/10.1021/ic201712e.
[89] G. Zhang, L. Wang, J. Pan, Probing the binding of the flavonoid Diosmetin to human serum albumin by multispectroscopic techniques, J. Agric. Food Chem. 60 (2012) 2721–2729, https://doi.org/10.1021/jf205260g.
[90] A. Varshney, P. Sen, E. Ahmad, M. Rehan, N. Subbarao, R.H. Khan, Ligand binding strategies of human serum albumin: how can the cargo be utilized? Chirality 22 (2010) 77–87, https://doi.org/10.1002/chir.20709.
[91] I. Petitpas, A.A. Bhattacharya, S. Twine, M. East, S. Curry, Crystal structure analysis of warfarin binding to human serum albumin, J. Biol. Chem. 276 (2001) 22804–22809, https://doi.org/10.1074/jbc.M100575200.
[92] E. Lazaro, P.J. Lowe, X. Briand, B. Faller, New approach to measure protein binding based on a parallel artificial membrane assay and human serum albumin, J. Med. Chem. 51 (2008) 2009–2017, https://doi.org/10.1021/jm7012826.
[93] S.L. French, M.L. Sikes, R.D. Hontz, Y.N. Osheim, T.E. Lambert, A. El Hage, M.M. Smith, D. Tollervey, J.S. Smith, A.L. Beyer, Distinguishing the roles of topoisomerases I and II in relief of transcription-induced torsional stress in yeast rRNA genes, Mol. Cell. Biol. 31 (2011) 482–494, https://doi.org/10.1128/MCB.00589-10.
[94] K. Gokduman, Strategies targeting DNA topoisomerase I in cancer chemotherapy: camptothecins, nanocarriers for camptothecins, organic non-camptothecin compounds and metal complexes, Curr. Drug Targets 17 (2016) 1928–1939, https://doi.org/10.2174/1389450117666160502151707.
[95] G. Capranico, J. Marinello, G. Chillemi, Type I DNA topoisomerases, J. Med. Chem. 60 (2017) 2169–2192, https://doi.org/10.1021/acs.jmedchem.6b00966.
[96] S.G. Churusova, D.V. Aleksanyan, E.Y. Rybalkina, O.Y. Susova, V.V. Brunova, R.R. Aysin, Y.V. Nelyubina, A.S. Peregudov, E.I. Gutsul, Z.S. Klemenkova, V.A. Kozlov, Highly cytotoxic palladium(II) pincer complexes based on picolinylamides functionalized with amino acids bearing ancillary S-donor groups, Inorg. Chem. 56 (2017) 9834–9850, https://doi.org/10.1021/acs.inorgchem.7b01348.
[97] A. Aydın, S. Aslan Korkmaz, V. Demir, S. Tekin, Anticancer and cytotoxic activities of $[Cu(C_6H_{16}N_2O_2)_2][Ni(CN)_4]$ and $[Cu(C_6H_{16}N_2O_2)Pd(CN)_4]$ cyanidometallate compounds on HT29, HeLa, C6 and vero cell lines, Anti Cancer Agents Med. Chem. 17 (2017) 865–874, https://doi.org/10.2174/1871520617666170103102417.
[98] A.M.A. Velásquez, W.C. Ribeiro, V. Venn, S. Castelli, M.S. de Camargo, R.P. de Assis, R.A. de Souza, A.R. Ribeiro, T.G. Passalacqua, J.A. da Rosa, A.M. Baviera, A.E. Mauro, A. Desideri, E.E. Almeida-Amaral, M.A.S. Graminha, Efficacy of a binuclear cyclopalladated compound therapy for cutaneous Leishmaniasis in the murine model of infection with Leishmania amazonensis and its inhibitory effect on topoisomerase 1B, Antimicrob. Agents Chemother. 61 (2017) e00688-17, , https://doi.org/10.1128/AAC.00688-17.
[99] F.V. Rocha, C.V. Barra, S.S. Garrido, F.A. Manente, I.Z. Carlos, J. Ellena, A.S.C. Fuentes, A. Gautier, L. Morel, A.E. Mauro, A.V.G. Netto, Cationic Pd(II) complexes acting as topoisomerase II inhibitors: synthesis, characterization, DNA interaction and cytotoxicity, J. Inorg. Biochem. 159 (2016) 165–168, https://doi.org/10.1016/j.jinorgbio.2016.02.039.
[100] C.V. Barra, F.V. Rocha, L. Morel, A. Gautier, S.S. Garrido, A.E. Mauro, R.C.G. Frem, A.V.G. Netto, DNA binding, topoisomerase inhibition and cytotoxicity of palladium(II) complexes with 1,10-phenanthroline and thioureas, Inorganica Chim. Acta. 446 (2016) 54–60, https://doi.org/10.1016/J.ICA.2016.02.053.
[101] M. Zhu, X. Cui, S. Zhang, L. Liu, Z. Han, E. Gao, The structures, cytotoxicity, apoptosis and molecular docking controlled by the aliphatic chain of palladium(II) complexes, J. Inorg. Biochem. 157 (2016) 34–45, https://doi.org/10.1016/j.jinorgbio.2016.01.016.
[102] B.L. Staker, M.D. Feese, M. Cushman, Y. Pommier, D. Zembower, L. Stewart, A.B. Burgin, Structures of three classes of anticancer agents bound to the human topoisomerase I-DNA covalent complex, J. Med. Chem. 48 (2005) 2336–2345, https://doi.org/10.1021/jm049146p.
[103] N.R. Filipović, S. Bjelogrlić, T.R. Todorović, V.A. Blagojević, C.D. Muller, A. Marinković, M. Vujčić, B. Janović, A.S. Malešević, N. Begović, M. Senćanski, D.M. Minić, Ni(II) complex with bishydrazone ligand: synthesis, characterization, DNA binding studies and pro-apoptotic and pro-differentiation induction in human cancerous cell lines, RSC Adv. 6 (2016) 108726–108740, https://doi.org/10.1039/c6ra24604d.